Korean J. Chem. Eng., 40(1), 11-36 (2023)
DOI: 10.1007/s11814-022-1316-8
pISSN: 0256-1115
eISSN: 1975-7220

REVIEW PAPER

Comprehensive review on physical properties of supercritical carbon dioxide calculated by molecular simulation

Gaoliang Liao*,, Yuntao Du*,**, Feng Zhang*,**,†, and Jiaqiang E*,****

*College of Mechanical and Vehicle Engineering, Hunan University, Changsha 410082, China
**Institute of New Energy and Energy-saving & Emission-reduction Technology, Hunan University, Changsha 410082, China
(*Received 31 May 2022 • Revised 2 September 2022 • Accepted 11 October 2022*)

Abstract−The applications of molecular simulation in supercritical carbon dioxide (S-CO_2) and its mixtures are reviewed. First, an overview of physical properties of S-CO_2 and CO_2 models is given. Secondly, the accuracy of S-CO_2 thermodynamic and transport properties calculated by different models is compared. It shows that Zhang's model has relatively better global accuracy in calculating thermodynamic properties. EPM2, Zhang and Cygan models have similar accuracy when calculating transport properties based on equilibrium molecular simulation (EMD) method, but generally have higher deviations when calculating thermal conductivity. Therefore, EMD and non-equilibrium molecular simulation (NEMD) methods have been compared in calculating thermal conductivity. The results show that NEMD is better than EMD but the process is complicated. The structural properties are also discussed in this part. Thirdly, the applications of molecular simulation in S-CO_2 binary organic, binary inorganic and multiple mixtures are reviewed. Finally, the summary and the prospect of future works are given.

Keywords: Molecular Simulation, Supercritical Carbon Dioxide, Thermodynamic Properties, Transport Properties, Mixtures

INTRODUCTION

Computational science has become the third largest branch of science after experimental science and theoretical science owing to the rapid development of computer technology and theory. Molecular simulation, as one of the most widely used technologies in computational science, has been developed for more than 60 years, which can be traced back to 1957 when Alder and Wainwright investigated the motion of molecular systems from 32 to 500 hard spheres [1-3]. So far, molecular simulation has been extensively applied in many fields as shown in Fig. 1, including biological science [4-7], mechanics [8-10], geological engineering [11], physics [12-15], and material science [16-19]. Therefore, a large number of applications of molecular simulation in various disciplines have proven that it is invaluable for studying a variety of complex physical, chemical, and biochemical systems and predicting the physical chemical properties of fluids for the following reasons:

(1) Molecular simulation can be utilized as one of the alternative methods of experiments which often spend a great deal of manpower and material resources.

(2) We can directly look into the microscopic properties of matter through molecular simulation, which are hard to observe experimentally because of the limitation of the temporal-spatial scale.

(3) Molecular simulation depends little on experimental data and has better predictability than such thermodynamic models as an equation of state (EOS) [20].

(4) Molecular simulation can solve problems that cannot be addressed by theoretical analysis, and connect theory and experiment via numerical calculation and simulation technology.

(5) Molecular simulation is an atomic-scale method that can describe the physical or chemical process from atomic level to give us a better interpretation of experimental results. In particular, a force field which governs the interaction between particles must be constructed for molecular dynamics (MD) simulation and the "realism" of the simulation outcome to represent the actual system depends directly on the accuracy of the force field. Consequently, establishing a new force field and continuously optimizing the force field is always an issue worthy of attention in various fields. For supercritical carbon dioxide (S-CO_2), a variety of force fields have been set up and concluded by Stubbs [21].

Supercritical fluids (SCFs), that is, substances whose both temperature and pressure are above the critical values, have received widespread attention and applications as a new safe and efficient "green solvent" in recent decades for their suitable density, solvent, transport properties [22-24]. S-CO_2 has become the most widely applied SCF in many fields such as S-CO_2 power cycle [25], extraction and separation process [26-29] and chemical reaction [30], because it is nontoxic, non-flammable, inexpensive, inert, non-corrosive, easily recyclable and has a mild critical point of which temperature is 30.98 °C and pressure is 7.38 MPa, respectively. What is more, the physical chemical properties of S-CO_2, for instance, density, viscosity, diffusion coefficient, dielectric constant, are very sensitive to the variation of temperature and pressure, especially near the critical point, which means that it will vary drastically once the temperature or pressure changes slightly. Hence, we can obtain its ideal properties by appropriately adjusting the operating temperature and pressure in the supercritical region.

So far, many applications of molecular simulation have been

†To whom correspondence should be addressed.
E-mail: fengzhang@hnu.edu.cn

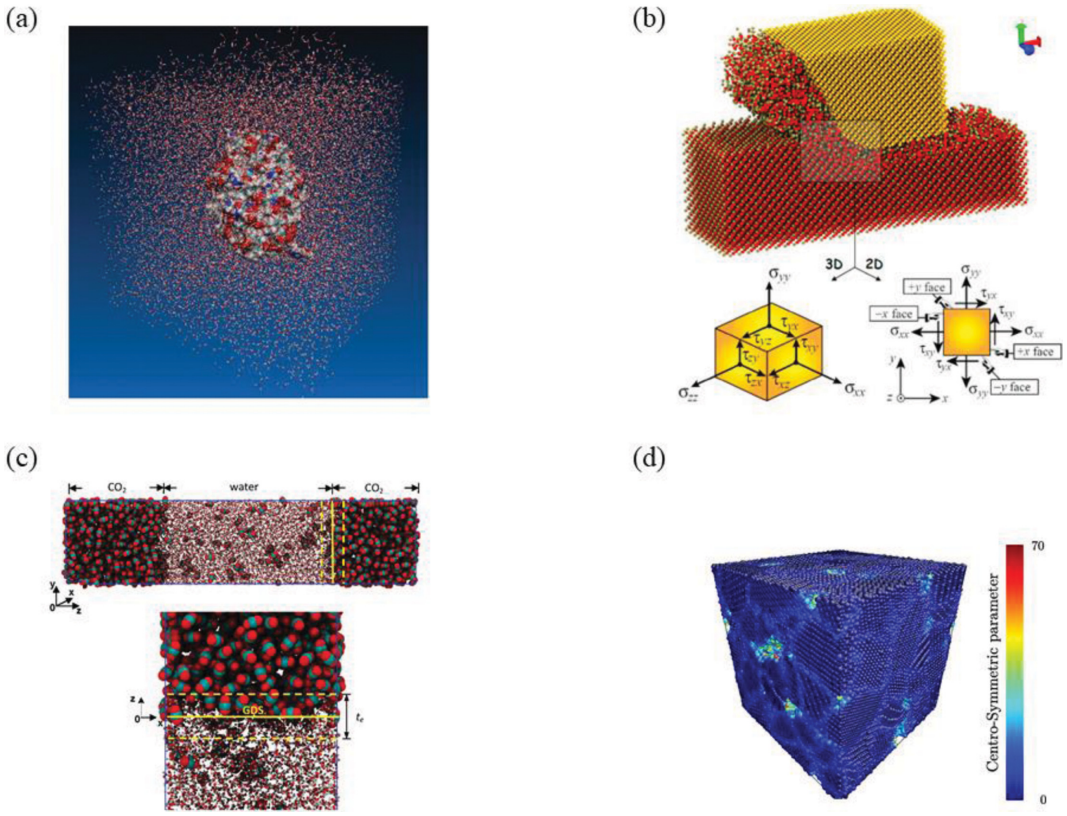

Fig. 1. The application of molecular simulation in various fields. (a) A typical cubic simulation box with protein in the center surrounded by solvent atoms (water) [5]; (b) Schematic representation of machining stress in the cutting zone [9]; (c) Schematic diagrams showing simulation snapshot of a CO_2-water binary mixture and details of the interface [13]; (d) The box contains 403076 aluminum atoms and sizes 19.3 nm edge [18].

applied to research related to the S-CO_2 such as characterizations of its structure, predictions of its thermophysical property, complements of its experimental data, studies of CO_2 solution [21]. Though a number of molecular simulations have been used in S-CO_2, to the author's knowledge, there are only few reviews on the applications of molecular simulation in the S-CO_2. Zhang et al. [31] reviewed the simulation methods and results of pure SCFs, which mainly were S-CO_2 and supercritical water in different applications, including bulk and confined space, supercritical extraction and reaction. At the end of the article, the authors also discussed the new trends and the new problems which need to be solved in these fields. Stubbs [21] conducted a start on understanding and carrying out molecular simulations on SCFs. In his article, molecular models and simulation methodologies were introduced and the studies of SCFs covering water, aqueous solutions, CO_2, CO_2 solutions and other SCFs with molecular simulations were reviewed in detail. Finally, limitations and future prospects of molecular simulation were given. These reviews included the applications of molecular simulation in S-CO_2 from various aspects, but did not include many new researches in these fields emerging rapidly in recent years, and S-CO_2 was only reviewed as a part of SCF. Furthermore, the author has not found any specific reviews for S-CO_2 about applications of molecular simulation to date, so the aim of this article is to present a detailed review about applications of molecular simulation in S-CO_2 combining the latest research finds, as well as a review of the basic properties of S-CO_2.

The remaining sections of this paper are grouped as follows. Section 2 presents an overview of the properties of S-CO_2 and the CO_2 models. Section 3 reviews the application of molecular simulation in calculating thermodynamic, transport and structural properties of S-CO_2 pure fluids. Section 4 considers the application of molecular simulation in S-CO_2 mixture fluids, including organic, inorganic and multicomponent mixtures. In section 5, summary and future work are presented.

THE PHYSICAL PROPERTIES OF S-CO_2 AND CO_2 MODELS

1. The Research Progress of Physical Properties of S-CO_2

S-CO_2 is a substance whose physical properties, such as density, viscosity and diffusion coefficient, are between liquid and gas phase, with its properties changing dramatically in the vicinity of the critical point. In this part, several thermodynamic properties and transport properties of S-CO_2 are reviewed.

Fig. 2 to Fig. 11 show the thermodynamic and transport properties of S-CO_2 near the critical point. Fig. 2 shows the relationship between density and temperature and pressure. It can be seen that density is very sensitive to temperature and pressure changes near the critical point, and this sensitivity weakens when it is far from the critical point. The density increases with the increase of pres-

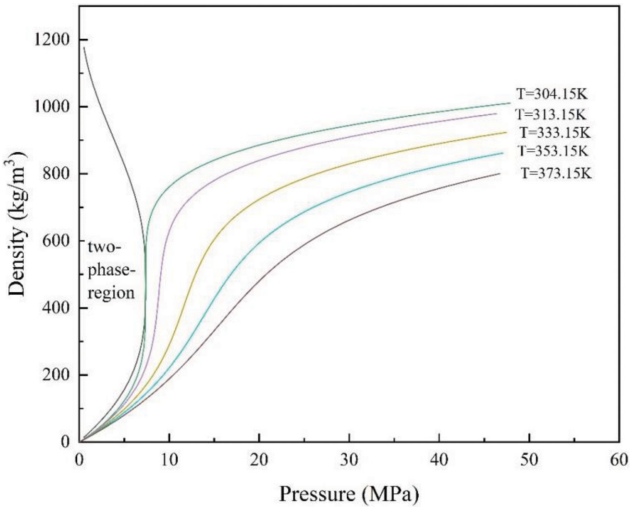

Fig. 2. Diagram of density variation of carbon dioxide with pressure (Data from NIST).

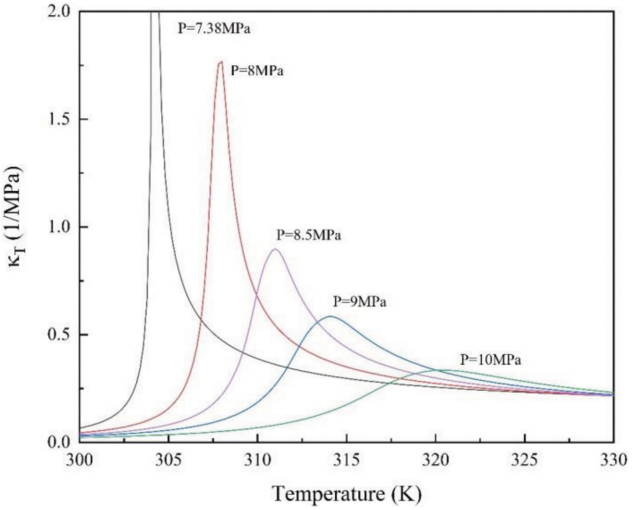

Fig. 4. Diagram of isothermal compressibility variation of carbon dioxide with temperature.

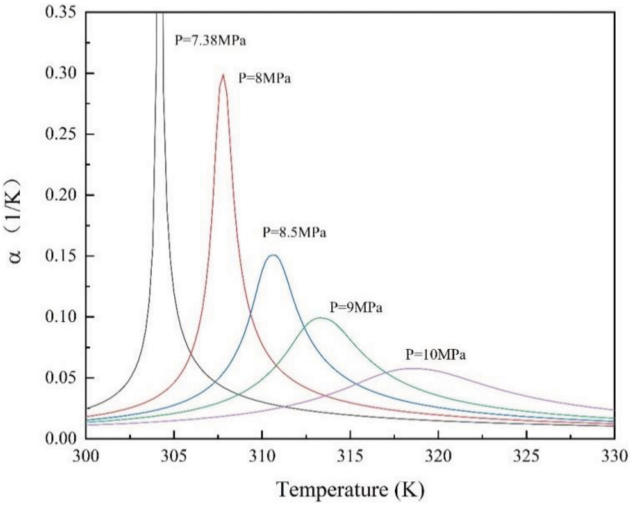

Fig. 3. Diagram of volume expansivity variation of carbon dioxide with temperature.

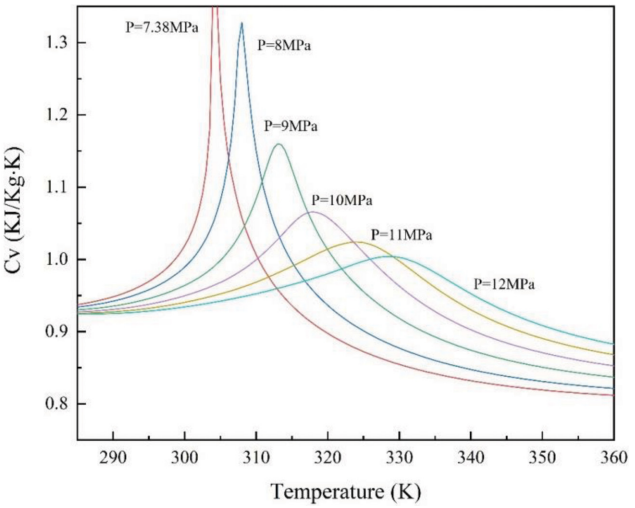

Fig. 5. Diagram of isochoric heat capacity variation of carbon dioxide with temperature.

sure and decreases with the increase of temperature. Furthermore, density, as one of the most important properties of S-CO_2, is closely related to other properties, such as a linear correlation with the change of solubility [32]. Many researchers have to date studied the thermodynamic properties of carbon dioxide near the critical point and provided reliable data [33-41]. Koppel and Smith [33] used their experimental apparatus to measure the enthalpy of CO_2 in the critical region, extrapolating the isobaric heat capacity and entropy, and their results showed that, with some errors, they were more accurate than previously available. Beck et al. [35] calculated the isochoric heat capacity at subcritical density, near critical density and supercritical density by measuring relevant parameters with a C_v-calorimeter of small dimensions, and determined the critical exponent. The results obtained were in good agreement with the calorimetric results obtained by predecessors. The volume expansivity, isothermal compressibility, isochoric heat capacity and isobaric heat capacity of S-CO_2 have similar characteristics with the change of temperature, and all have a peak value that decreases with the increase of pressure as shown in Fig. 3 to Fig. 6. It can be seen from Fig. 7 that the Joule-Thomson coefficient also has a peak value in the supercritical region, and this peak value increases as it approaches the critical point. Speed of sound is also an important property for S-CO_2 (see Fig. 8). Estrada-Alexanders and Trusler [40] measured the propagation velocity of sound waves along seven isotherms (From 220 to 450 K) in CO_2 using a spherical resonator and obtained both second and third virial coefficients, and volumetric second virial coefficients. They found that pure CO_2 had severe vibration relaxation at a frequency of the order 10 kHZ when the pressure was less than 1 MPa, which limited the measurement accuracy, but there was still an overall estimate. Later, Liu et al. [41] measured the sound speed of gaseous CO_2 along the isotherm (From 260 to 333 K) with a cylindrical resonator. They corrected

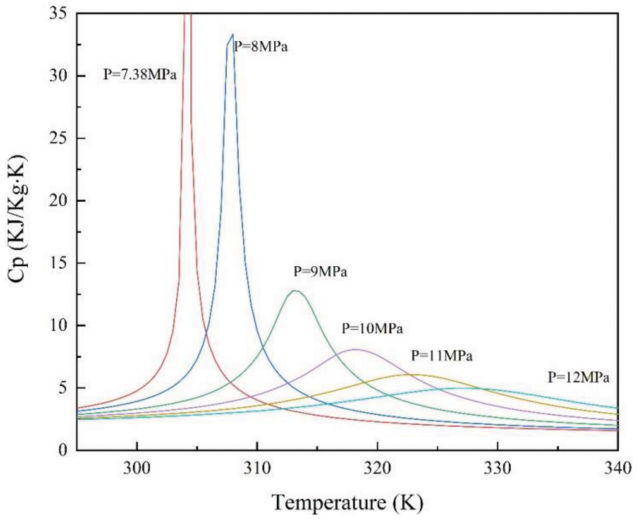

Fig. 6. Diagram of isobaric heat capacity variation of carbon dioxide with temperature.

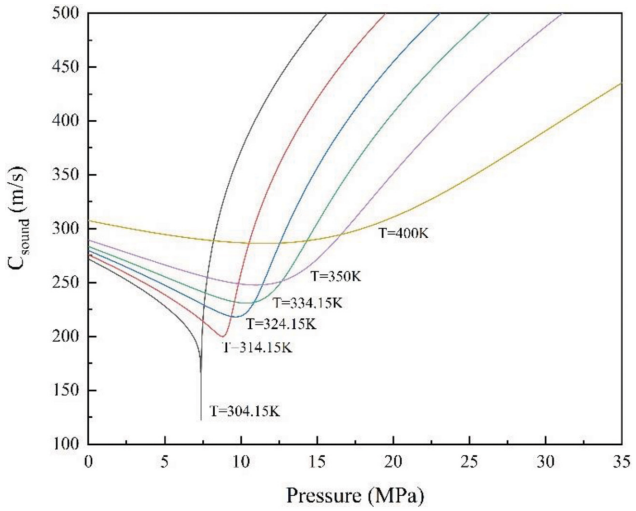

Fig. 8. Diagram of speed sound variation of carbon dioxide with pressure.

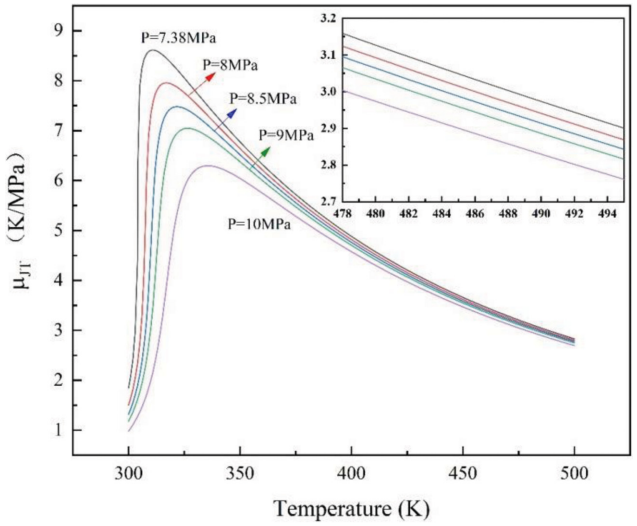

Fig. 7. Diagram of Joule-Thomson coefficient variation of carbon dioxide with temperature.

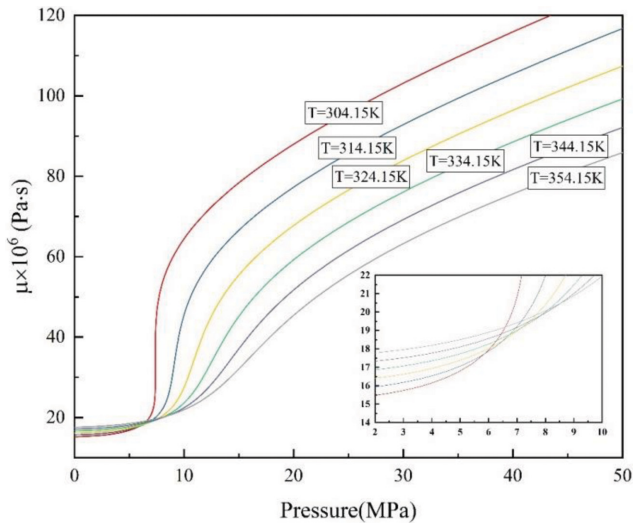

Fig. 9. Diagram of viscosity variation of carbon dioxide with pressure.

various disturbances in frequency measurement, such as the thermal and viscous boundary disturbances, the gas fill duct disturbance and the vibrational relaxation disturbance. The relative standard uncertainty they measured was estimated to be less than 0.02%, and within this uncertainty the measured values were consistent with the results of Estrada-Alexanders and Trusler [40].

The researchers also provide much reliable information on transport properties in the critical region of S-CO_2 [42-47]. As for the viscosity, Fig. 9 shows the viscosity of S-CO_2 as a function of pressure. From Fig. 9, we can conclude that the viscosity changes dramatically near the critical point, and the severity of such changes decreases with the rise of temperature (that is, away from the critical point). Lasesecke and Muzny [48] collated and compiled a comprehensive database of experimental and computational CO_2 data and established a new reference correlation with better accuracy and covering a wider range of pressures and temperatures. Fig. 10 shows the thermal conductivity of S-CO_2 as a function of density. It can be seen that the thermal conductivity has a peak value at critical density, which decreases with the rise of temperature and is very sensitive to the temperature. Huber et al. [49] summarized the data of thermal conductivity of CO_2 measured by predecessors, and deduced a new and representative equation of thermal conductivity of CO_2 based on a large number of experimental data. Unlike thermal conductivity, thermal diffusivity also varies significantly near critical points but is insensitive to temperature changes as shown in Fig. 11.

More information on the properties of S-CO_2 has been reviewed by Polikhronidi et al. [50]. In their paper, the structural, thermodynamic and transport properties of S-CO_2, including pure fluid and mixture fluid, as well as the technical and scientific applications of S-CO_2 in natural and industrial engineering, have been

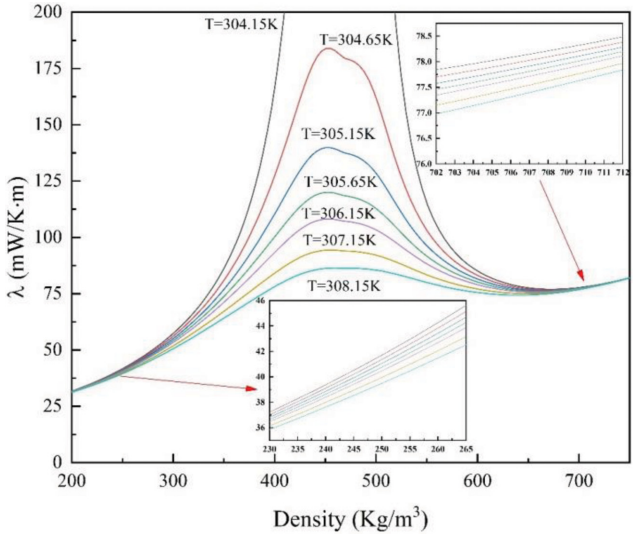

Fig. 10. Diagram of thermal conductivity variation of carbon dioxide with density.

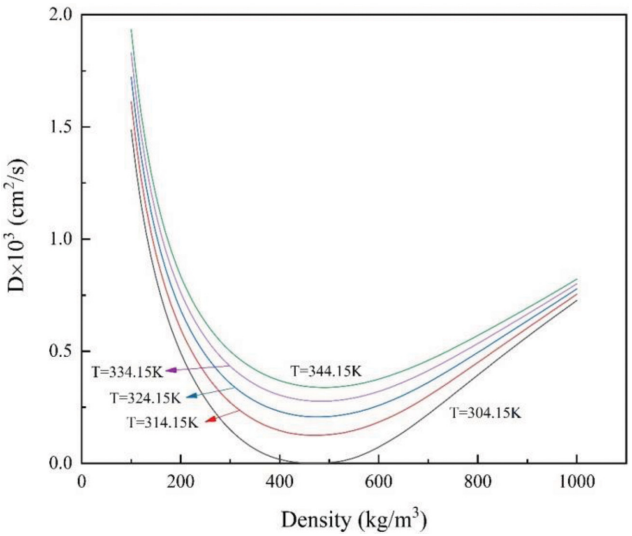

Fig. 11. Diagram of thermal diffusivity variation of carbon dioxide with density.

reviewed. In general, the properties of S-CO_2 all change dramatically around the critical point, and molecular simulation can provide a range of microscopic explanations compared to experiments.

2. CO_2 Models

We here introduce several typical potential energy models and CO_2 structural models, and explain their related applications.

Potential energy is used to describe the interaction between molecules, and a combination of multiple potential energies is called a force field. The potential energy model of molecules with complex structures is often decomposed into bonded and non-bonded interactions. Bond interactions generally include bond stretching, bond angle bending, dihedral angle distortion, as shown in Fig. 12. The most common non-bonding potential energy is Lennard-Jones (LJ) potential energy due to the van der Waals (vdWs) interactions, also known as 12-6 potential energy, which is often used to model dispersion-repulsion interactions. Its equation is as follows:

$$U_{LJ}(r_{ij}) = 4\varepsilon_{ij}\left[\left(\frac{\sigma_{ij}}{r_{ij}}\right)^{12} - \left(\frac{\sigma_{ij}}{r_{ij}}\right)^{6}\right] \quad (1)$$

where r_{ij}, ε_{ij}, σ_{ij} are the separation, LJ well depth, LJ size, respectively, for the pair of atoms i and j. If atoms i and j are different atoms, then the potential energy constants ε and σ of LJ are expressed by Eq. (2) and Eq. (3), respectively, through Lorentz-Berthelot combining rules [51]. The application of LJ potential energy model in CO_2 is of great significance [52-54]. Bouanich [52] used LJ potential energy model plus dipole and quadrupole interactions to obtain

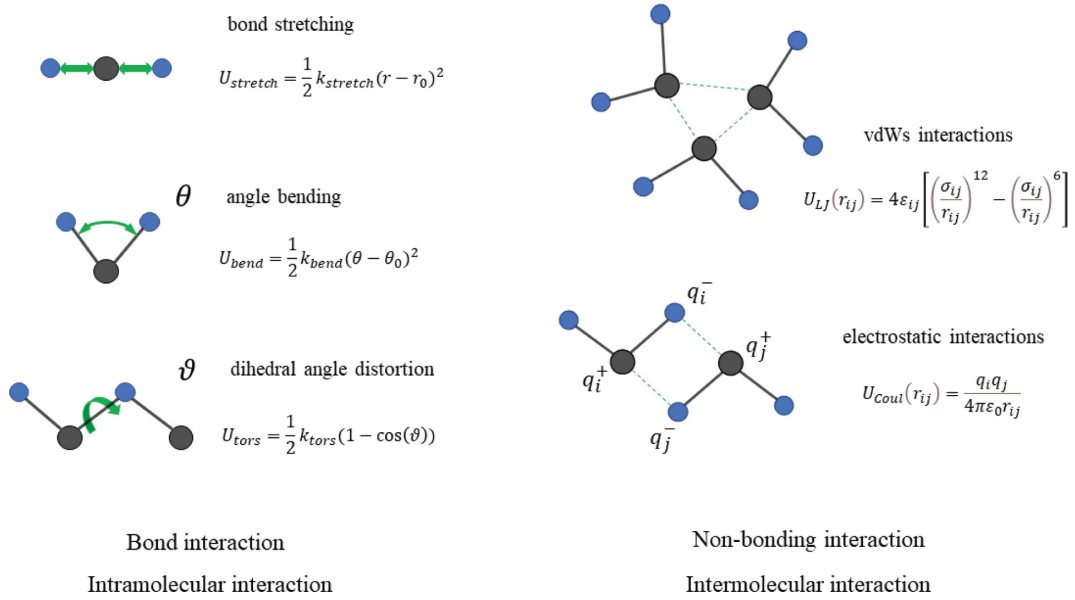

Fig. 12. Schematic representation of intramolecular and intermolecular interaction.

the second-virial coefficient of CO_2 molecules and its site-site LJ parameters. Steele and Posch [54] used two versions of three-site LJ model with an ideal quadrupolar interaction to study the induced infrared absorption in CO_2 liquid phase and concluded that the change of LJ parameters has great influence on the research results.

$$\sigma_{ij}=\frac{\sigma_i+\sigma_j}{2} \tag{2}$$

$$\varepsilon_{ij}=\sqrt{\varepsilon_i\varepsilon_j} \tag{3}$$

Another common non-bonding interaction is Coulomb interaction. Atoms on some molecules may have partial charges, which will lead to electrostatic interactions. The strength of the interaction depends on the value of the partial charges carried by the atoms. For example, in general, for neutral molecules, the partial charges on the atoms are small enough to ignore the coulomb interaction. The Coulomb potential is shown in the following equation:

$$U_{Coul}(r_{ij})=\frac{q_iq_j}{4\pi\varepsilon_0 r_{ij}} \tag{4}$$

where q_i, q_j and ε_0 are the partial charges of atoms i and j, vacuum permittivity, respectively. These potential energies are pairwise additive to each other, regardless of bonded or non-bonded. Models with partial charges usually consider both LJ and Coulomb interactions [51,54,55], and flexible terms are added if the models are flexible [56,57].

In addition to dividing molecular interaction into bonded and non-bonded interactions, they can also be decomposed into short-range interactions and long-range interactions, according to the distance of the range of interaction between molecules. LJ interaction and Coulomb interaction are typical short-range interaction and long-range interaction, respectively. When short-range interactions are considered, truncation of distant intermolecular interactions will not lead to obvious errors, while when long-range interactions are considered, truncation cannot be done, because it will lead to large errors due to long distance interactions [58]. Although there is no essential difference between them, they will be treated separately in the MD algorithm. So far, most of the models are still empirical, and much of the optimization of the models is only achieved by changing the field parameters, such as molecular bond length, bond angle and LJ parameters. However, there is no one kind of model that can be applied to any condition. The existing models under the certain physical conditions such as temperature and pressure compared with the experimental only in some properties are well fitting, so the researcher's aim is that force field parameters can be applied to a wider range of a series of physical conditions and the mixture.

For CO_2, a large number of models have been developed and are constantly being optimized. Two- or three-site models with an additional point quadrupole moment, which were proposed and compared by Murthy, Singer, and McDonald (MSM) [59,60], are the popular structure models of CO_2, showing good prediction of various properties, except that the two-site model is somewhat inaccurate in describing its dynamic properties of the crystal [59]. Since then, a number of new potential models can be regarded as the descendants of MSM [20,61-66]. Among them, Harris and Yung's model [62] called elementary physical model (EPM) and its variant EPM2 have been widely concerned and used by researchers. Their models have three LJ sites with charges centered at each atom. Their results showed that EPM2 had good predictability in the critical region. The models of Zhang and Duan [20] are also popular and are rigid three-site LJ interaction and Coulomb interaction models with partial charges, which have good predictability and transferability in volumetric properties and phase behavior. Several models also focus on vapor-liquid equilibria (VLE) [62,67-70]. For example, the TraPPE model, proposed by Potoff and Siepmann [67], which is also rigid three-site LJ interaction with each partial charge on LJ site, shows high accuracy in calculating CO_2 VLE. Merker et al. [70] proposed a model consisting of three LJ sites and one quadrupole moment with good accuracy in saturated density, vapor pressure, shear viscosity and thermal conductivity.

At present, most CO_2 models are rigid, linear and the bond length is fixed, because rigid models are simple in form and the execution time of the flexible model calculation is about 30% longer than the rigid model [65]. However, to approximate a more realistic state, it is necessary to build CO_2 flexible models [57,62,71-74]. Zhu et al. [57] developed a fully flexible model to predict the vapor-liquid coexistence and structural properties. Their results showed that in supercritical state, the structure of CO_2 molecules is not linear and its bond angle is 176.4°, which also explains why S-CO_2 has a dipole moment. The nonlinear model of CO_2 proposed by Zhang et al. [74] combined the nonlinearity of CO_2 with classical EPM and EPM2 models [62] to calculate the thermodynamic properties, dielectric constant and structure of S-CO_2. Nieto-Draghi et al. [71] modified the EPM2 model with the semiflexible and fully flexible versions to calculate shear viscosity and thermal conductivity of S-CO_2, but the results had large deviations. To further study the linearity of CO_2, Anderson et al. [75] introduced a rigid linear CO_2 model, which included the allowable fluctuation of bond angle with both consideration of LJ and Coulombic interactions, to study the bond angle distribution in gas and supercritical state. It can be seen that in the supercritical region, the CO_2 properties are very different from those of vapor-liquid phase and numerous models for supercritical state will also be established.

The single site model and the two-site model are also very meaningful for CO_2 modeling. The single spherical site with LJ interaction is the simplest model of CO_2. Its advantage lies in computational efficiency and easy parameterization by statistical theories from experimental data of various properties. Higashi et al. [53] used this model to calculate the transport properties of aromatic compounds in supercritical fluids, which agreed well with experimental data. However, the single site model cannot adequately describe the vapor-liquid coexistence curve and molecular microstructure information. Avendano et al. [76] proposed a single site model without Coulomb interaction; instead, the potential was based on the use of SAFT-VR Mie EOS. The two-site model can be dated back to 1974 when Gibbons and Klein [77] introduced it with Mie potential interaction to investigate the thermodynamic properties of CO_2. Since then, CO_2 models with two-site have been continuously optimized to study various properties of CO_2 [59,68,78,79]. John and Shaw et al. [78] developed a two-site model of force acting on oxygen atoms, with an exponential-6 potential to reflect the repulsive-

dispersive interaction. Chacin et al. [79] proposed a two-site model plus point quadrupole with LJ interaction to model fluid-fluid interaction.

However, the potential energy model composed of LJ interaction and Coulomb interaction of simple-point charge cannot completely reproduce the actual properties of CO_2, and the neglect of many-body polarization effects is one of the important reasons. Therefore, many researchers proposed new CO_2 polarization models on the basis of predecessors in order to incorporate the polarization effect into the potential energy model [80-83]. Persson et al. [80] developed the polarizable three-site rigid potential energy model, which reproduced the experimental second and third virial coefficients within only a few percent, showing a significant improvement compared to the simple pair interaction potentials with an error of nearly 20%. Wang et al. [82] proposed a distributed point polarizable model and also predicted the second virial coefficients well. For chemical reaction systems containing CO_2, the classical force field is obviously not applicable because of bond breaking and formation. Hence, some reactive models of CO_2 have also been proposed [84].

In addition to the empirical site-site model, another way to obtain potential energy parameters is to use *ab initio* quantum mechanical calculations [85-91]. For this model, the partial charges are not at the LJ sites, which is different from the EPM-type model [76]. Within the author's knowledge, there are many CO_2 models not mentioned in this article, and the author has found several other models for interested readers to refer to [92-96]. There are also several references comparing classical CO_2 models for calculating different properties under certain conditions [21,97-99]. Either the TraPPE or Zhang and Duan models are superior to other models based on various considerations such as model transferability to other molecules and applicability to mixture systems [21].

THE APPLICATIONS OF MOLECULAR SIMULATION IN S-CO_2 PURE FLUID

1. Thermodynamic Properties

1-1. Fluctuation Theory

The density (ρ) of the simulated system is computed by means of the ensemble average ($\langle V\rangle$) of the system volume according to ρ=NM/($N_a\langle V\rangle$) [98], where N is the number of molecules in the simulated system, M is the molecular weight and N_a is Avogadro's number. The fluctuation theory under NPT ensemble is one of the commonly used methods to calculate the thermodynamic properties of fluids in simulation. It was first derived by Lagache et al. [100,101], and then applied to CO_2 [76,98,102,103]. According to the fluctuation theory, volume expansivity (α) and the isothermal compressibility (k_T) can be computed from following expressions with proper unit conversion:

$$\alpha=\frac{\langle VH_{conf}\rangle-\langle V\rangle\langle H_{conf}\rangle}{\langle V\rangle k_B T^2} \tag{5}$$

$$k_T=\frac{\langle V^2\rangle-\langle V\rangle^2}{\langle V\rangle k_B T} \tag{6}$$

where k_B is the Boltzmann constant, H_{conf} is the configurational enthalpy (which excludes the kinetic and intramolecular terms), and, $H_{conf}=U_{conf}+PV$, where U_{conf} is the potential energy of the system due to the intermolecular interaction (when the CO_2 model is rigid, U_{conf} is the total potential energy since no intramolecular terms are considered), P and T is the thermodynamic pressure and temperature, respectively, and the angle brackets indicate ensemble averages.

In fluctuation theory, isobaric heat capacity is divided into two parts to better compare experimental data: $C_p=C_p^{res}+C_p^{id}$, where C_p^{id} is defined as the ideal contribution that can be taken from experimental correlations [104], C_p^{res} is calculated from the following expressions:

$$C_p^{res}=\frac{\langle U_{conf}H_{conf}\rangle-\langle U_{conf}\rangle\langle H_{conf}\rangle}{k_B T^2}+\frac{\langle VH_{conf}\rangle-\langle V\rangle\langle H_{conf}\rangle}{k_B T^2}-Nk_B \tag{7}$$

Once these properties are determined, the second derivative properties can then be calculated using standard thermodynamic relationships. The isochoric heat capacity C_v, the Joule-Thomson coefficient μ_{JT} and speed of sound C_{sound} can be computed conveniently from the following expressions:

$$C_v=C_p-\frac{T\langle V\rangle\alpha^2}{k_T} \tag{8}$$

Table 1. Several commonly used Force field model parameters

		EPM2	TraPPE	Zhang	EPM2-flex	TraPPE-flex	Cygan	Higashi	SAFT-γ
ε/Kcal·mol^{-1}	C-C	0.0558	0.0536	28.845[a]	0.0558	0.0536	0.0559	236.10[a]	361.69[a]
	O-O	0.1599	0.1569	82.656[a]	0.1599	0.1569	0.1596		
σ_{ij}/A	C-C	2.757	2.800	2.7918	2.757	2.800	2.800	3.7200	3.7410
	O-O	3.033	3.050	3.000	3.033	3.050	3.028		
q/e	C	+0.6512	+0.7000	+0.5888	+0.6512	+0.7000	+0.6512	-	-
	O	−0.3256	−0.3500	−0.2944	−0.3256	−0.3500	−0.3256	-	-
r_0/A	C-O	1.149	1.160	1.163	1.149	1.160	1.162	-	-
θ_0/°	C-O	180.0	180.0	180.0	180.0	180.0	180	-	-
k_r/kal mol^{-1} A^{-2}		-	-	-	2,565.547	2,057.096	2,017.033	-	-
k_θ/kcal mol^{-1} rad^{-2}		-	-	-	295.2804	111.9509	107.9589	-	-
Reference		[62]	[67]	[20]	[71]	[72]	[73]	[53]	[76]

[a]K

$$\mu_{JT}=\left(\frac{\partial T}{\partial P}\right)=\frac{\langle V\rangle(T\alpha-1)}{C_p} \tag{9}$$

$$C^2_{sound}=\frac{C_p}{C_v k_T \rho} \tag{10}$$

1-2. Comparison of Force Field Models for Calculating Thermodynamic Properties

The CO_2 force field model enormously determines the accuracy of thermodynamic property calculation results. Table 1 lists the parameters of commonly used CO_2 force field models, including three-site rigid models (EPM2, TraPPE, Zhang), three-site flexible models (EPM2-flex, TraPPE-flex, Cygan) and two single-site models (Higashi, SAFT-γ). Aimoli et al. [98] compared the accuracy of seven kinds of CO_2 force field models in calculating thermodynamic properties. Average absolute deviation (AAD) is a parameter that measures the degree of deviation between simulated results and experimental data from the NIST, expressed as follows:

$$AAD=\frac{1}{n_T}\sum_{t=1}^{n_T}\left|\frac{A_t^{NIST}-A_t^{CALC}}{A_t^{NIST}}\right|100\% \tag{11}$$

where A_t^{CALC} is the predicted result from the MD simulation, A_t^{NIST} denotes the reference data from NIST, and n_T represents the summation runs over all temperatures at a given pressure. From the study by Aimoli et al., we can see that three-site rigid model shows better accuracy compared with other models, and three-site flexible models show great deviation. Among three-site rigid models, all of these models have similar accuracy. Overall, Zhang's model is slightly more accurate. Fig. 13 compares the AAD values predicted by three-site rigid model, SAFT-γ, and the Peng-Robinson equation of state (PR-EOS) over different temperature ranges. As we can see from Fig. 13, as mentioned earlier, there is no one model that can be applied to accurately predict any property parameters. They are only well fitted within a certain pressure or temperature range, so they have limitations. But it also means that you can choose the right model based on the target pressure or temperature range. At the same time, comparing the results of molecular simulation with PR equation of state, we can see that molecular simulation is as accurate as, or even more accurate than, PR-EOS in some temperature or pressure ranges. Yang et al. [103] compared the accuracy of several force field models in predicting thermodynamic properties of pure CO_2 system, and the results showed that TraPPE-flex model performed best in predicting isobaric and isochoric heat capacities. The accuracy of predicting isobaric heat capacity is similar to PR-EOS, but the accuracy of PR equation is worse than TraPPE-flex force field model when calculating isochoric heat capacity. Therefore, for calculating the heat capacity of CO_2 mixture, TraPPE-flex force field would be more suitable.

1-3. Vapor-liquid Equilibrium (VLE)

The separation process in the chemical industry requires a full understanding of the phase behavior of pure fluids or mixtures, such as VLE, so that it can meet the requirements of the product in practice, especially for natural gas liquefaction and refrigeration applications [105]. EOS is one of the traditional methods for dealing with the calculation of VLE properties in chemical engineering. The EOS model is generally based on pure phase properties and can only produce qualitative prediction of VLE in binary and ternary mixtures. To express quantitatively, it is necessary to intro-

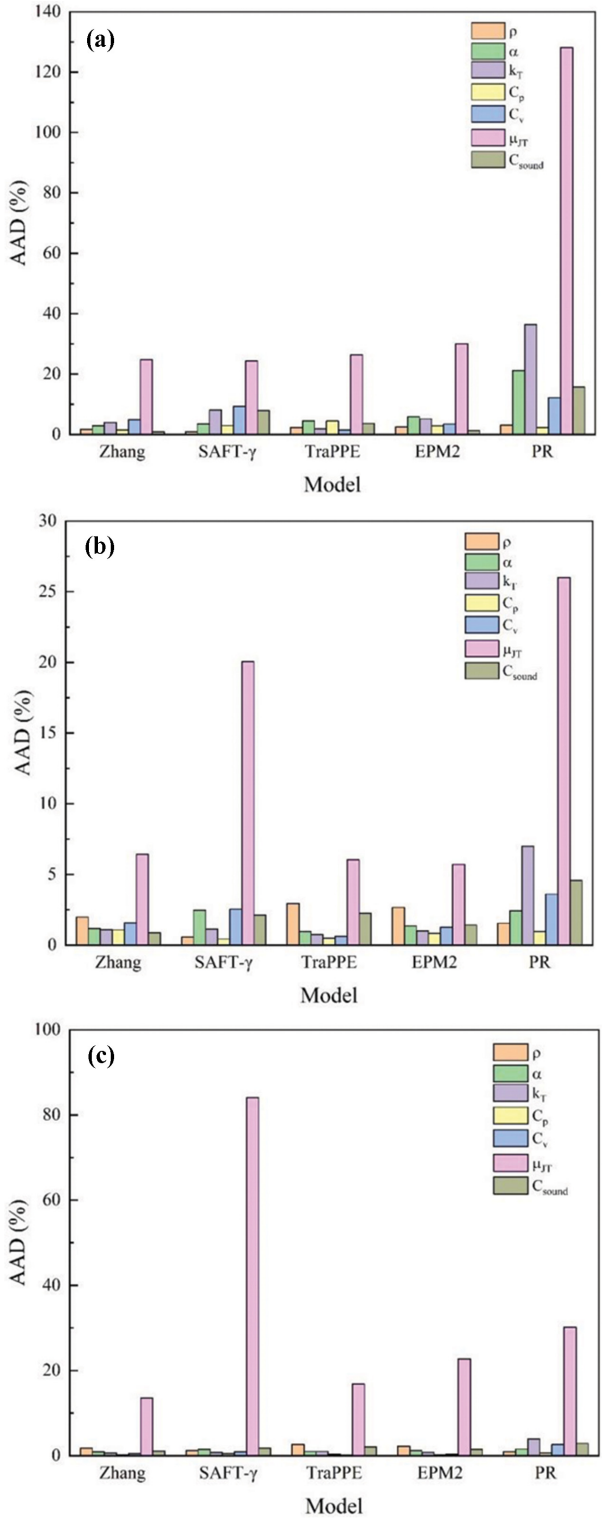

Fig. 13. Force field model comparison of AAD in predicting thermodynamic properties over (a) 300-480 K, (b) 500-680 K, (c) 700-900 K temperature ranges, respectively, at 20 K intervals (Data from the study of Aimoli et al. [98]. See Table S1 in supplementary data).

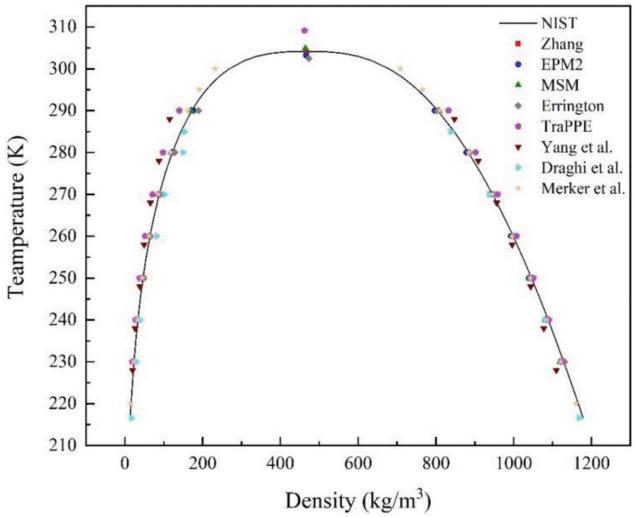

Fig. 14. Comparison of saturation density calculated by several models with NIST (Data from the references [20,70,71,105]. See Table S2).

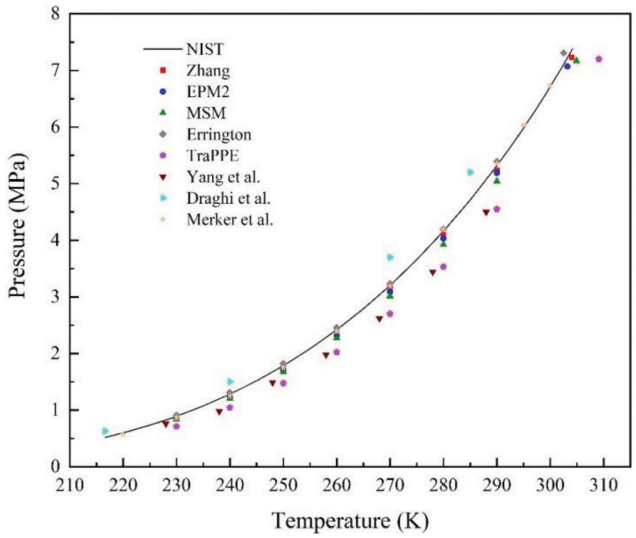

Fig. 15. Comparison of saturation vapor pressure calculated by several models with NIST (Data from the references [20,70,71, 105]. See Table S2).

duce empirically derived binary interaction parameters [67]. Because of its simple form, few parameters, and fast calculation speed, EOS has been widely used in chemical engineering practice [104,106]. However, the dependence on experiments leads to great limitation of the EOS model, such as the inability to deal with the calculation of thermal properties of thermodynamic properties of complex fluids due to the lack of experimental data. To make up for the shortcoming of EOS modelling, molecular simulation can not only deal with the calculation of thermodynamic properties of complex fluids, but also has a relatively high accuracy in the results as long as there is an accurate and transferable force field. Yang et al. [105] compared the accuracy of molecular simulation and four EOS models in predicting the VLE properties of CH_4, CO_2 and their binary mixtures, and the results showed that molecular simulation and PC-SAFT EOS had good adaptability to both pure and mixed systems, and could obtain satisfactory prediction for all saturation properties. For accurately describing the VLE characteristics of CO_2 in molecular simulation, the force field models developed for it are gradually enriched, such as two center Lennard-Jones plus point quadrupole model by Moller and Fischer [68] and EPM2 model [62] in the early stage. Vrabec et al. [69] presented Moller and Fischer variations, and the calculated VLE properties were in good agreement with experimental values. Potoff and Siepmann derived the TraPPE model suitable for CO_2 and N_2 by optimizing EPM2 model to calculate VLE characteristics as shown in Fig. 14 and Fig. 15. The model developed by Zhang and Duan [20] has high accuracy in calculating VLE characteristics of CO_2. Meanwhile, they also compared the accuracy of the model with other models in calculating VLE properties, as shown in Fig. 14 and Fig. 15.

Zhang and Duan's model is accurate in predicting many thermal properties and it could be a strong candidate to describe the accurate and highly transferable force field for CO_2. But still, it also shows relatively poorer performance than other models at some thermodynamic ranges [20]. Nieto-Draghi et al. [71] introduced a flexible version of EPM2 to calculate the VLE coexistence curve of CO_2. Merker et al. [70] summarized the characteristics of the previous model for calculating VLE characteristics and formulated their own model based on the VLE data. Their model had comparable accuracy with the model presented by Vrabec et al. in terms of saturation density and vapor pressure. In recent years, Chen et al. [107] compared the accuracy of calculation of CO_2 vapor-liquid coexistence curve by several models. Fig. 14 and Fig. 15 show the comparison of the predicted results of mentioned models with NIST values in terms of saturation density and saturation pressure, respectively. It can be concluded from these figures that both EPM2 and Zhang's model have a better global prediction of VLE properties. For Zhang's model, the average relative deviation of saturated liquid density, saturated vapor density and saturation pressure is 0.1%, 2.3% and 0.7%, respectively, and the prediction accuracy of saturated liquid density and saturation pressure is the highest. The accuracy of saturated vapor density is second only to 1.7% predicted by EPM2 model. TraPPE, Yang et al.'s model and Nieto-Draghi et al.'s model has large average relative deviation in predicting saturated vapor density and saturation pressure, which is 18.6%, 17.9%, 18.9% and 18.7%, 12.6%, 16.1% respectively. The prediction accuracy of other models is in the middle of these, among which EPM2 model is excellent, and the prediction on accuracy of saturated liquid density, saturated vapor density and saturation pressure is 0.7%, 1.7% and 3.9% respectively. In summary, Zhang's model and EPM2 model are recommended for calculating VLE properties.

2. Transport Properties

2-1. Methodology

The transfer of mass, heat and momentum of fluid in industrial engineering compels us to pay attention to the transport properties of fluids, and predicting the transport properties of fluids of interest in industry is also one of the main motivations for MD simulation [108]. At present, two methodologies are mainly used to calculate fluid transport properties, such as viscosity, thermal conductivity and diffusion coefficient. One is the combination of

equilibrium molecular dynamics (EMD) and Green-Kubo relations [109,110], and the other is the non-equilibrium molecular dynamics method (NEMD).

According to the Green-Kubo relations, the transport characteristic coefficients of momentum and energy flows in non-equilibrium states can be expressed by the decay of equilibrium fluctuation of pressure and heat flux [99]. Green-Kubo relations are a kind of formula that relates the transport coefficients of the non-equilibrium process to the fluctuation of the corresponding physical quantity in the equilibrium states, which can be understood that the transport coefficients are equal to the integral of the self-correlation function over the correlation time. For example, the diffusion coefficient D is the integral of the velocity self-correlation function; The shear viscosity μ is the integral of the pressure self-correlation function. The thermal conductivity λ is the integral of the self-correlation function of heat flux. They are shown as follows [108]:

$$D=\frac{1}{3N}\int_0^\infty \sum_{i=1}^{N}\langle V_i(t)\cdot V_i(0)\rangle dt \tag{12}$$

$$\mu=\frac{V}{k_BT}\int_0^\infty \langle P_{\alpha\beta}(t)P_{\alpha\beta}(0)\rangle dt \tag{13}$$

$$\lambda=\frac{V}{3k_BT^2}\int_0^\infty \langle J(t)\cdot J(0)\rangle dt \tag{14}$$

where V and T are the volume and temperature of the system, respectively, k_B is the Boltzmann constant and N is the total number of the atoms in the system. $V_i(t)$, $P_{\alpha\beta}(t)$, J(t) represent the velocity of particle i, pressure tensor component and heat flux respectively. α and β represent any pair of Cartesian coordinates x, y and z. The angle brackets represent the equilibrium ensemble average of the system self-correlation function. For diffusion coefficients D, in some cases it may be more appropriate to use the Einstein relation [111]:

$$D=\frac{1}{6}\lim_{t\to\infty}\langle|r_i(t)-r_i(0)|^2\rangle \tag{15}$$

where $r_i(t)$ is the atomic coordinate vector, and the term inside the angle brackets is the mean square displacement (MSD). In this method, the self-diffusion coefficient is proportional to MSD as a function of time in the diffusion region. Meanwhile, the coefficient is the average value along the three-dimensional space x, y and z.

NEMD makes the system out of equilibrium by modifying the boundary conditions of the simulated system (i.e., adding disturbances), and then obtains the transport coefficient from various thermodynamic relationships [112,113]. For example, heat conduction is the phenomenon of energy transfer caused by a temperature gradient, which belongs to a non-equilibrium process. NEMD first establishes a temperature gradient through some method, such as momentum exchange [114], velocity rescaling [115,116], local heat bath, etc., and waits for a long enough time to make the system reach steady state. After that, the temperature gradient and non-equilibrium heat flux of the system are measured, and then the thermal conductivity can be calculated according to Fourier's law:

$$\lambda=-\frac{J}{A\times\nabla T} \tag{16}$$

where A and ∇T are the transfer area and the temperature gradient, respectively. Heat flux J and temperature gradient ∇T can be measured directly from the simulation:

$$J=\frac{\partial E}{\partial t} \tag{17}$$

$$\nabla T=\frac{\partial T}{\partial x} \tag{18}$$

where E and t are the input energy and the input time, respectively. x is the displacement of heat transfer direction. It is also convenient to calculate other transport properties such as viscosity using NEMD [113,117].

EMD and NEMD have their own advantages and disadvantages [58]. The combination of EMD simulation with linear theory or time-correlation function allows EMD to simultaneously calculate various transport properties such as thermal conductivity, viscosity and diffusion coefficient, but the calculation accuracy of this method is not ideal. For linear response theory, it is only applicable to the linear corresponding region with small external disturbance and close to the equilibrium region, and not suitable for the nonlinear corresponding region with large external disturbance and far from the equilibrium region. For the time-correlation function, it only reflects the response of the system property to a small disturbance, which is tiny compared with the random disturbance widely existing in the system, so its calculation accuracy is limited. Moreover, the spatial size applicable to EMD simulation system also limits the maximum correlation time of time-correlation function. NEMD adopts a method similar to the experimental measurement of the transport coefficient. First, various disturbances are added to the simulated system, such as heat flow, material flow, and momentum flow, and then the response of the simulated system to the disturbance is recorded. Finally, the viscosity, thermal conductivity, diffusion coefficient, etc., of the system are calculated according to the corresponding relationships. The calculation accuracy of NEMD is higher than that of EMD, because the system can improve the calculation accuracy as long as the disturbance is large enough, and the system can enter the nonlinear response region far from equilibrium, which overcomes the limitation of linear response theory. In addition, the calculation accuracy of time-correlation function can be greatly improved by prolonging the simulation time. Generally, NEMD is more effective than EMD method, but the problem suitable for NEMD is specific, that is, each transport coefficient needs to be simulated separately, which increases the difficulty of the simulation. EMD method is more efficient than NEMD method for calculating multiple transport coefficient simultaneously for a particular fluid [108].

2-2. Comparison of Force Field for Calculating Transport Properties

Suitable method and high-precision CO_2 model can better predict the transport properties. The three transport properties of viscosity, thermal conductivity and diffusion coefficient are often paid attention in industry and are also commonly used indicators to test the accuracy of the CO_2 model. The lack of experimental data under extreme conditions requires molecular simulation to extend existing CO_2 models to a wider thermodynamic range, or to establish new models for extreme conditions. Previously, many researchers compared the classical CO_2 model used to calculate transport

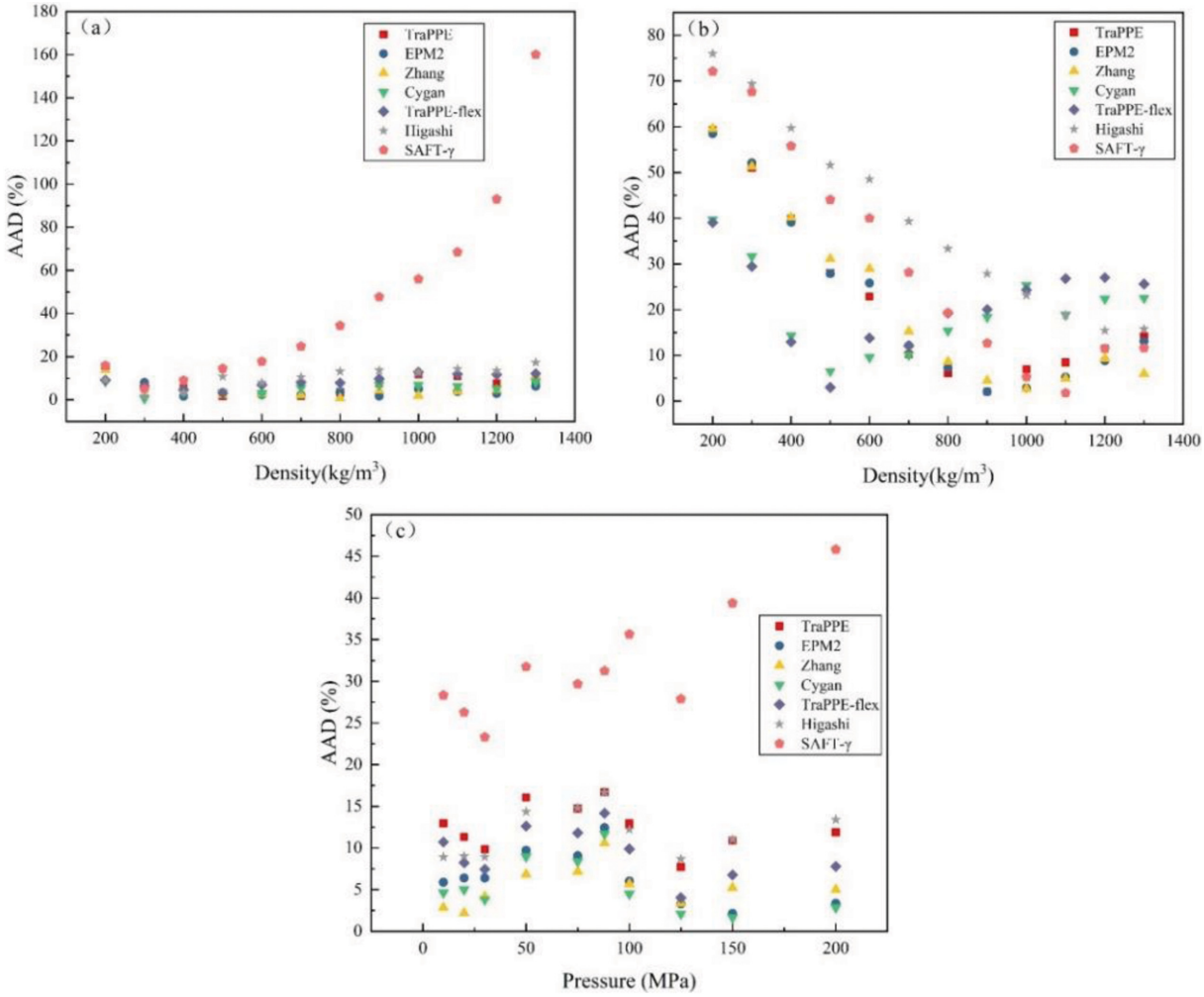

Fig. 16. AAD comparison of temperature of each model at certain density or pressure: (a) viscosity, (b) thermal conductivity, (c) diffusion coefficient. The temperature range of viscosity and thermal conductivity is 273.15-573.15 K, and the temperature range of diffusion coefficient is 273-450 K (Data from Aimoli et al. [99]. See Table S3).

properties in a wider thermodynamic range [99,118]. The famous one is the study of Aimoli et al. [99], who compared the deviation of seven classical models in calculating transport properties by EMD method, including three three-site rigid models (EPM2, Zhang, TraPPE), two three-site flexible models (Cygan, TraPPE-flex) and two single-site models (Higashi, SAFT-γ), which are consistent with the calculation of CO_2 thermodynamic properties [98]. Their simulation ranged in temperature from 273.15 to 573.15 K, in density from 200 to 1,300 kg/m^3, and in pressure up to 200 MPa. This part focuses on the deviation of predicted transport properties between CO_2 models, so the deviation will appear in the form of AAD, as shown in Eq. (11). The simulation results of Aimoli et al. are shown in Fig. 16 to Fig. 18. The comparative study of Zhong et al. [118] focused on the comparison of flexible models, and their study extended the simulated temperature range to a lower 223 K-450 K.

In terms of viscosity, according to the comparison results of Aimoli et al., as shown in Fig. 16(a) and Fig. 17(a), all models are not sensitive to density and temperature changes, with basically a deviation of less than 20%, except that the SAFT-γ model changes dramatically when the density is greater than 600 kg/m^3 and the temperature is between 273.15-300 K. In Fig. 18, the global deviation of EPM2, Zhang and Cygan is similar. EPM2's global deviation of 4.69% is slightly better than Zhang's 4.99% and Cygan's 5.62%. Zhong et al. reached a different conclusion when the simulated range was reduced to 223 K-450 K. Zhong et al. used a transverse-current correlation functions (TACFs) method [119,120] different from Green-Kubo relation to calculate viscosity, and the results showed that EPM2-flex had the best global prediction of viscosity, but was poor at low temperatures such as 223 K and 243 K. However, the TraPPE-flex model had better performance at low temperatures.

As for thermal conductivity, as shown in Fig. 16(b) and Fig. 17(b), all models deviated greatly in the range of low density, which was alleviated in the range of high density, and the accuracy of prediction was inferior to other properties, as shown in Fig. 18. This can also indicate that EMD method has low accuracy in calculating thermal conductivity. Except that the deviation value is low at low temperature, the models are not very significant for temperature change. The three-site models are generally better than the single-site models, but the SAFT-γ model is not much different from the

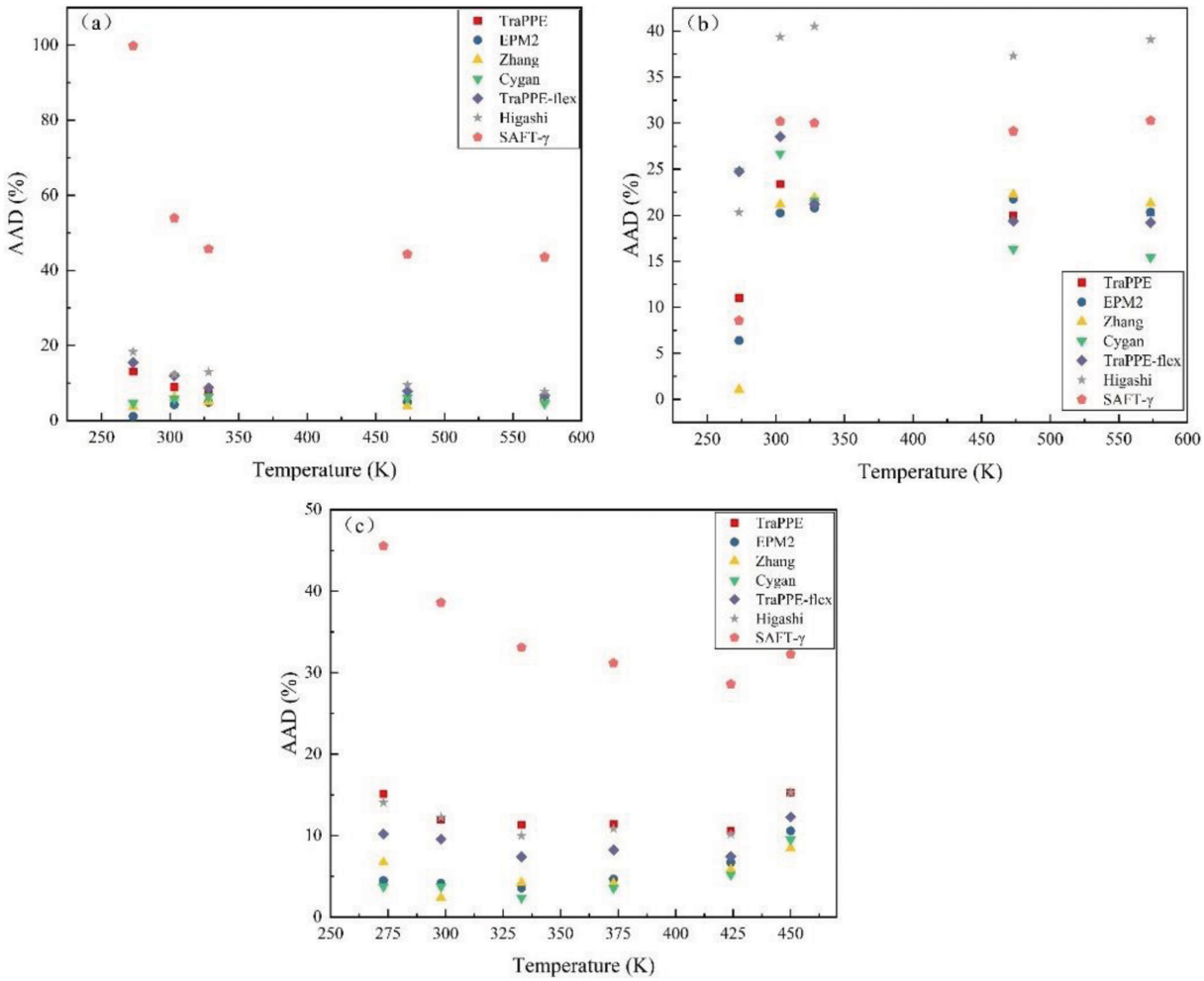

Fig. 17. AAD comparison of density or pressure of each model at certain temperature: (a) viscosity, (b) thermal conductivity, (c) diffusion coefficient. The density range of viscosity and thermal conductivity is 200-1,300 kg/m^3, and the pressure range of diffusion coefficient is up to 200 MPa (Data from Aimoli et al. [99]. See Table S4).

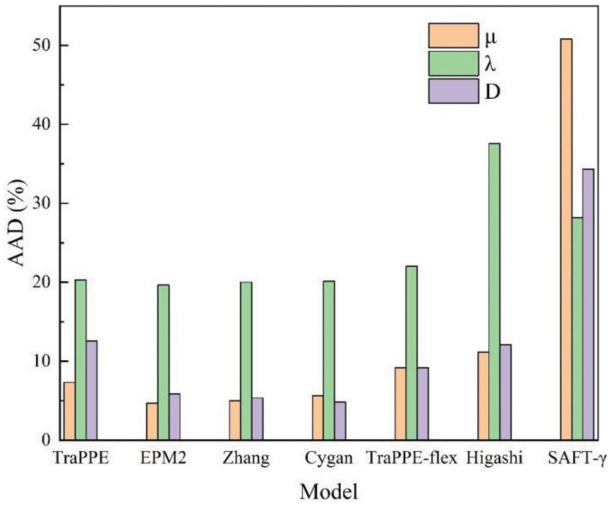

Fig. 18. Global AAD comparison of transport properties predicted by 7 models: viscosity (orange), thermal conductivity (green), self-diffusion coefficient (purple) (Data from Aimoli et al. [99]. See Table S5).

three-site model in high density. In addition to using EMD method, researchers also focus on NEMD method to calculate thermal conductivity [71,107,121-124]. Chen et al. [107] calculated the self-diffusion coefficient of CO_2 by Einstein relation and the thermal conductivity of CO_2 by NEMD, respectively. Table 2 illustrates the comparison of AAD for calculating thermal conductivity between EMD and NEMD. It can be seen that at high density, the AAD obtained by using NEMD method to calculate thermal conductivity is significantly smaller than that obtained by using EMD method. This is shows that NEMD method is obviously better than EMD method in calculating thermal conductivity. Nieto-Draghi et al. [71] used multiple versions of EPM2 to calculate transport properties, including rigid, semi-flexible (variable bond angle), fully flexible (variable bond angle and variable bond length) versions. Shear viscosity using Einstein relation and thermal conductivity was calculated by NEMD method. The results show that all versions are consistent with experimental values at high density, although there is a slight deviation. However, at low density, the deviation of all versions increases significantly, which is consistent with the situation when Aimoli et al. calculated thermal conductivity using EMD

Table 2. The AAD comparison of calculated thermal conductivity between EMD and NEMD

Chen et al. (250 K)		
Density (kg/m^3)\model	Cygan	TraPPE_flex
1055	15	6.6
1137	14.3	4.6
1218	10.8	5.6
Global	13.4	5.6
Aimoli et al. (273.15 K)		
Density (kg/m^3)\model	Cygan	TraPPE_flex
1000	28.6	17.3
1100	20	23.8
1200	22.2	26.9
Global	23.6	22.7

method. After that, Merker et al. [70] developed their own model based on Vrabec et al's model [69] and calculated the transport properties of CO_2 using EMD method. By Comparing the model of Vrabec et al., the self-diffusion coefficient predicted accuracy was improved. The AAD of viscosity and thermal conductivity are within the same error range compared with Nieto-Draghi et al., indicating that the calculation deviation of thermal conductivity by using EMD method in Merker et al's model is the same as that by using NEMD in Nieto-Draghi et al's EPM2 model. This may indicate that although EMD method is not suitable for calculating thermal conductivity, EMD method can also achieve the accuracy of NEMD method as long as the model is precise enough.

Considering the self-diffusion coefficient, note that the experiment values compared by Aimoli et al. are those measured by Groβ [125], as he has the widest temperature range of 223-450 K and pressure range of 10-200 MPa. It can be seen from Fig. 16(c) and Fig. 17(c) that SAFT-γ model has significant deviations in various pressure and temperature ranges, while the changes of pressure and temperature have little influence on the deviation of other models. The accuracy of Cygan model was the highest, with AAD of 4.85%, followed by EPM2's 5.87% and Zhang's 5.35%. The AAD of other models was between Cygan and SAFT-γ. The results of Zhong et al. showed that EPM2-flex had the highest accuracy of 6.83%, which was inferior to the Cygan model. They believed that temperature affected the performance of the model, so they explored the dependence of temperature and pressure on the model, and the results showed that temperature had a great influence on the model, which may be due to the low temperature range. For example, EPM2-flex and MSM-flex performed poorly at 223 K and 243 K, while TraPPE-flex performed well at low temperatures, consistent with what happened when calculating viscosity. The effect of pressure on the model is random, that is, there is a little correlation. In addition, He et al. [126] calculated the self-diffusion coefficient of CO_2 by COMPASS force field [127,128] using the Einstein relation, and compared it with the prediction equation of the self-coefficient of fluid based on the hard sphere model. The results showed that the mutual attraction and aggregation of fluid molecules reduced the diffusion capacity of fluids. Higashi and Tamura [129] used rigid and flexible versions of the EPM2 model to calculate the self-diffusion coefficient using Einstein's relation, and their simulation results agree well over a wide range of density.

In general, according to the comparison results of Aimoli et al., Zhang's model shows relatively better overall predicted satisfaction than other models when calculating each transport property, while according to the comparison results of Zhong et al., EPM2-flex model is much more predictive. This is probably because, as mentioned, they simulated different temperature ranges and used different calculation methods. Depending on the range of thermodynamics and actual conditions chosen, some models can sometimes show unrivalled accuracy in calculating transport properties, such as the Cygan model for predicting self-diffusion coefficient and TraPPE-flex for better prediction satisfaction at low temperatures.

3. Structural Properties

The structural properties of each model are also different. By studying the radial distribution function (RDF) characteristics of various models at temperature 273.15 K and density 1,300 kg/m^3, Aimoli et al. [99] concluded that without considering the influence of phase transition, the rigid (TraPPE, EPM2, Zhang) and flexible (TraPPE-flex, Cygan) three-site models have very similar liquid-like RDF. The reason for a little deviation between them is that the parameters of the force field are different, and the flexibility of the model has almost no effect on the liquid structure. There are two reasons for the large deviation of the single-site model [99]: first, its model structure. The united-atom model used for the single-site is quite different from the all-atom model used for the three-site. Although the united-atom model can promote dynamics better than all-atom model, it has the opposite effect at high density. The all-atom model under low density showed a low molecular mobility because in addition to have translation there will be other movement patterns, but in high density, the all-atom molecules due to the asymmetric system and free volume arising from the non-spherical structure have higher molecular mobility. In contrast, the united-atom model is surrounded by other atoms, resulting in low mobility. The second is the increased repulsion term. The repulsion properties of the SAFT-γ may promote the cage effect through stronger force equilibrium, thus imposing stricter restrictions on the molecular movement. The cage effect at high density indicates that these models begin to form glassy or semi-ordered structures prematurely, which leads to a decrease in molecular mobility as the system develops into solids. The cage effect in the single-site model is more significant than that in the multi-site model. The above is not limited to pure fluids, but is also possible for mixed fluids [130]. Conventional models generally regard CO_2 molecules as rigid linear molecules with O=C=O angle of 180°. However, much research has shown that CO_2 will turn nonlinear in the supercritical region and produce a dipole moment, although very small [57,74,131-134]. This is caused by the change of molecular geometry due to charge density polarization caused by intermolecular interaction [132], and S-CO_2 can show completely different properties at normal temperature and pressure, largely due to the particularity of its structure. Therefore, some classical models, such as EPM2 and TraPPE, may not be applicable in the supercritical region because they are rigid, and the S-CO_2 models have been gradually developed [57, 74]. Zhang et al. [74] studied a modified version of EPM2-M based on EPM model for calculating thermodynamic properties and

dielectric constant, and analyzed its structural characteristics. Satisfactory results can be obtained in the calculation of thermodynamic properties and dielectric constant, and the improvement in the calculation of dielectric constant is remarkable. Zhu et al. [57] developed a completely flexible model for the characteristics of VLE, and obtained acceptable results for the calculation results of various properties in the supercritical region, while the EPM2 model showed a large deviation in the supercritical state.

In addition to the linearity of a single CO_2 molecule, the study of the nearest neighbor structure of CO_2 molecular system is another key point. Experimental methods (neutron diffraction experiments [135-141] and X-ray diffraction experiments [142]) and molecular simulation [131-133,143-146] are both powerful means to explore the nearest neighbor structure of CO_2 molecular system. The radial distribution functions measured by different authors do not always agree on the uncertainty and statistical fluctuation involved in these experiments. It is generally believed that CO_2 nearest neighbor configuration can be divided into three types: parallel-slipped geometry, T-shaped geometry and crossed geometry, as shown in Fig. 19. Saharay et al. [132] used AIMD method to explore the reasons for the dissolution of various solute by S-CO_2 from the perspective of structure, and their results showed that the dipole moment generated by charge density polarization and existing reasonably ordered neighbor molecular structure at the state point with temperature of 318.15 K and density of 703 kg/m^3 can explain the ability of S-CO_2 to dissolve part of the solute, and the T-shaped geometry generated by the non-zero quadrupole moment a configuration of pairwise molecules. The T-shaped configuration dominates at a wide temperature and density, including supercritical region, and the T-shaped geometry begins to distort when the pressure rises. Thereafter, they varied pressure from 19 MPa to 500 MPa along the isotherm of 318.15 K to explore the structural and dynamic properties of pressure for S-CO_2 [131]. The results show that with the increase of pressure, the first coordination shell is remade and the twisted T-shaped arrangement between neighboring molecules around the central molecule changes gradually to the parallel-slipped geometry at a long distance. With the increase of pressure, the instantaneous O=C=O angular distribution tends to be linear, which may be caused by the depolarization of central molecules caused by the increase of coordination number at high density. By comparing their model with experimental values [136-138], Zhang and Duan [20] found that the atom-atom pair distribution function is sensitive to temperature and density changes. With the increase of temperature and decrease of density, the atom-atom pair distribution function generally widens with the decrease of the intensity of the first peak, which means that the characteristics of local structure weaken. But the weighting can "dilute" this strong dependence on temperature and density as the three pairs of distribution functions are added to the neutron-weighted distribution function. At low temperature and high density, a standard T-shaped geometry with perpendicular angles to the central molecule is preferred. As the temperature increases and the density decreases, the T-shaped structure gradually distorts due to thermal fluctuation, which is consistent with Saharay et al. [132]. The study of radial and angular correlation functions by Zhang et al. [74] shows that T-shaped dominates at different densities, which is also applicable to supercritical states, and other geometric configurations besides T-shaped geometry also exist in the first coordination shell. The energy of CO_2 dimer is almost the same as that of the parallel-slipped geometry, and the T-shaped structure is metastable. Because of the nonlinearity of supercritical state, CO_2 molecules also have concavity. The angular correlation function indicates that the probability of a molecule pointing towards the convex side of another molecule is equal to the probability of pointing towards the concave side, because the nonlinear behavior of CO_2 molecule is marginal only. These results are also consistent with Saharay et al. [132]. Furthermore, they found that at low density, structure is determined by attraction, while at high density, structure is determined by repulsion. Meanwhile, except for the structural features discussed above, in recent years, the structure of supercritical fluids is no longer considered to be single on the phase diagram, but there is a clear struc-

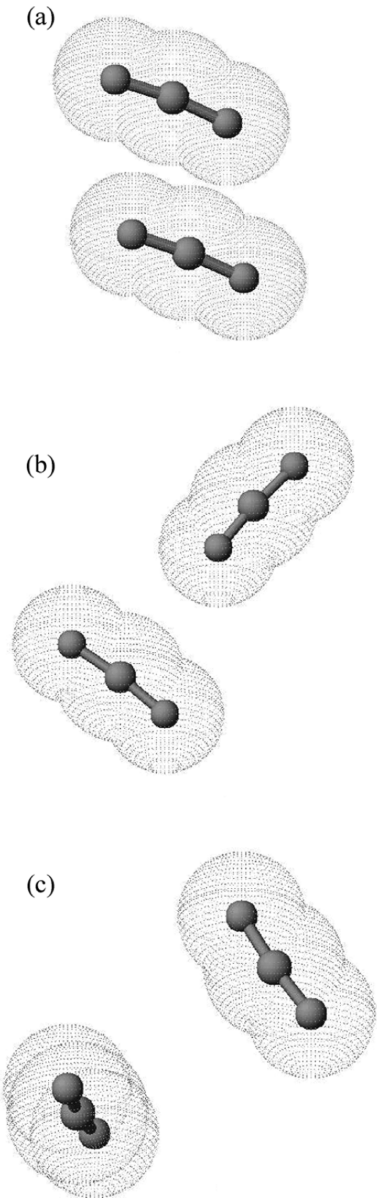

Fig. 19. Three nearest neighbor configurations of CO_2 [74]: (a) slipped-parallel, (b) T-shaped, and (c) crossed.

tural crossover. The structural crossover exists near the Frankel line, which was first brought by Brazhkin et al. [147] to make a distinction between liquid-like phase and gas-like phase. Bolmatov et al. [148] analyzed the one-component supercritical LJ fluid by MD simulation. They proved that the structure crossover demarcated liquid-like and gas-like configurations through the qualitative changes of distribution functions of interatomic distances and angles. More important, they found that this structure crossover was closely related to dynamics and thermodynamics. Later, they investigated the structure of S-CO_2 in the deep supercritical region [149]. They discovered the existence of persistent medium-range order correlations and proved the existence of an additional thermodynamic boundary in the supercritical carbon dioxide on an intermediate length scale. Brazhkin and his colleagues gave the Frenkel line of S-CO_2 from MD simulation [150] and, recently, using neutron scattering experiments and MD simulation, proved the structural crossover of S-CO_2 near the Frenkel line at 14 times reduced pressure by analyzing the structure factors and pair distribution functions [151]. This will promote our further understanding of structural properties in the supercritical region.

For the influence of quadrupole moment, many relevant studies have been done [97,152-157]. The importance of the quadrupole moment became apparent in the 1970s and 1980s, when it made sense to add it to simple spherical models. The differences in dispersion-repulsive interactions between classical rigid empirical rigid models are small, such as LJ parameter σ and bond length, which are usually less than 5%. It is mainly reflected in the Coulomb force, especially the charge difference between models, which usually reaches 20%-50%, and the charge difference is also reflected in the quadrupole moment, while non-zero dipole moment and large quadrupole moment have a great influence on the solubility and reaction rate of SCFs. Stapleton et al. [152] calculated vapor-liquid diagrams of pure and mixtures using MC simulation, and they found that the critical temperature of four-polar fluids increased rapidly with the increase of the strength of the quadrupole moment. Garzon et al. [153] used MC simulation to calculate VLE of different quadrupole Kihara fluids. By analyzing the influence of quadrupole moments on critical characteristics, they found the addition of quadrupole moments increased critical temperature, pressure and density, and the vapor-liquid coexisting curve became wider due to the addition of quadrupole. Mognetti et al. [157] used MC simulation to calculate the critical properties of a coarse-grained model of real four-polar fluids, and their results showed that the critical properties depended almost linearly on the quadrupole moment parameters. In addition to VLE, the quadrupole moment also has a great influence on liquid-solid equilibrium (LSE). Perez et al. [97] calculated the LSE of CO_2 using four models (Zhang, EPM2, MSM and TraPPE), focusing on the effect of the quadrupole moment. The results show that TraPPE model has the best description of the triple point and melting curve, and only the introduction of quadrupole moment in the solid phase can achieve stability. The melting temperature predicted by the four models is proportional to its own quadrupole moment. A lower quadrupole moment causes lower melting temperatures, while the highest quadrupole moment produces the best description, but all four models generally underestimate the melting temperature. Therefore, adding a quadrupole moment to the model can significantly improve the prediction of fluid properties, but this is not necessary [76,157].

In the supercritical region, when the molecular system is large enough, the aggregation of molecules cannot be ignored, especially when it is applied to supercritical extraction [158]. Ishii et al. [141] observed the aggregation state through using the snapshot of CO_2 system structure obtained by MD. In the case of high density, since the space is already full of CO_2 molecules, there is no extra space for local density fluctuation. When the density decreases, the number of molecules in the system decreases and there is more free space, so the local density fluctuation begins to increase, which leads to the molecular aggregation phenomenon being more obvious. Zhang et al. [74] took snapshots of two different densities along the isotherm (353.15 K), as shown in Fig. 20. At high density (745.5 kg/m^3), the molecular structure shows very small local density inho-

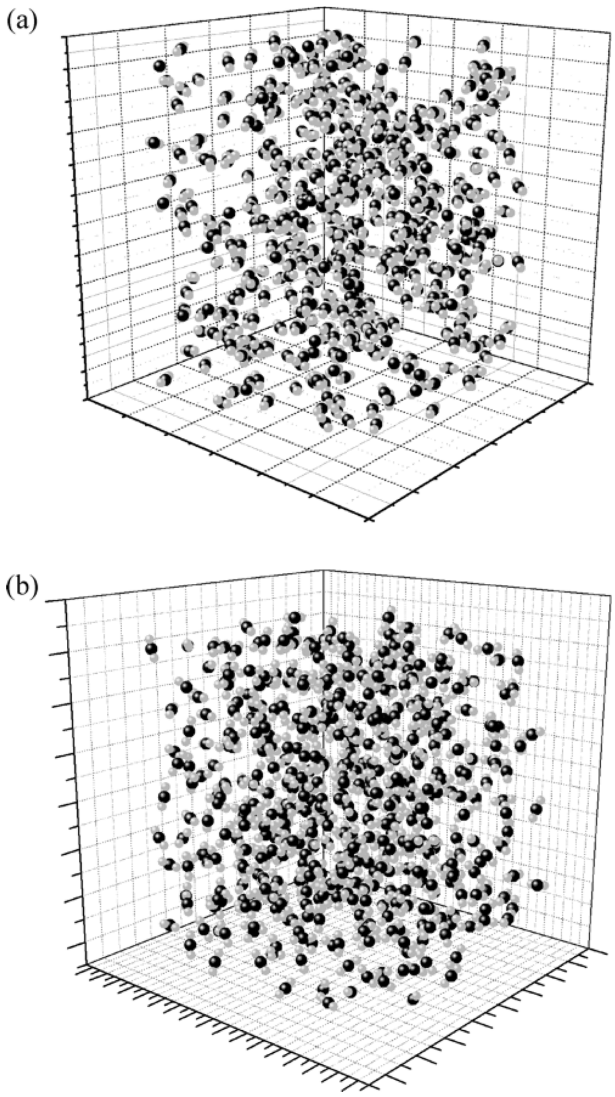

Fig. 20. Snapshots of 500 S-CO_2 molecules system obtained by Zhang et al. [74] through MC simulation along the isotherm curve (353 K). The gray is oxygen atom and the black is carbon atom. (a) Box length=61.1 Å, ρ=160.1 kg/m^3; (b) Box length= 36.6 Å, ρ=745.5 kg/m^3.

mogeneity because the molecules are very densely packed. In contrast, aggregation was more pronounced at relatively low density (160.1 kg/m^3). In a 3D diagram, large clusters can be found, indicating that strong local density inhomogeneity, which is consistent with the results obtained by Ishii et al. [140,141]. Except for pure CO_2 system, aggregation is also obvious in mixed systems [159, 160]. For example, Stubbs and Siepmann [159] studied the microstructure of S-CO_2 and methanol system by using TraPPE model and MC simulation. The effects of temperature, pressure, and density on the aggregation behavior and the strength of hydrogen bond between CO_2 and methanol were studied. The aggregation behavior of CO_2 mixtures will be discussed in detail in the next chapter.

THE APPLICATIONS OF MOLECULAR SIMULATION IN S-CO_2 MIXTURE FLUIDS

This section is divided into three sections by the types of mixtures: S-CO_2 organic fluids, S-CO_2 inorganic mixture fluids and S-CO_2 multicomponent mixture fluids. Note that for organic mixture fluids, we did not review all S-CO_2 mixture fluids, because of the large number of organic compounds, but selected representatives of organic compounds with simple molecular structure, including methane, methanol, ethane, ethanol, acetone and benzene. We will describe the use of molecular simulations in S-CO_2 mixtures fluids using these representatives. Similarly, for inorganic mixture fluids, we present water, ionic liquids (ILS) and common gases, including inert gases. Finally, we will describe several specific examples of multicomponent mixture fluids, including organic and inorganic mixture fluids.

1. S-CO_2 Organic Mixture Fluids

S-CO_2 has many advantages as a solvent compared with traditional organic solvents due to its non-toxicity, harmless source and low cost. This part will consider six organic solutes with simple molecular structure as representative of the S-CO_2 mixture system: methane, methanol, ethane, ethanol, acetone and benzene. The specific properties of S-CO_2 organic mixture fluids were investigated by using molecular simulations. Table 3 shows in detail the classification of relevant literature in different temperature and pressure ranges according to the composition of S-CO_2 binary system and the purposes of molecular simulation, including a small amount of non-critical region simulation (such as calculation of VLE).

To calculate the S-CO_2 organic mixture systems by molecular simulation, the force field used should be determined first. For CO_2, EPM2 and TraPPE are commonly used due to their early introduction and good fit for mixtures [62,67], while for organic solutes, selection should be made according to the characteristics of the target system to be calculated. Aimoli et al. [168] calculated the volume and second derivative properties of CO_2-methane system in the thermodynamic range of 323.15-573.15 K and 99.93 MPa by using MD simulation. They used TraPPE and SAFT-γ models for

Table 3. An overview of molecular simulation in S-CO_2 organic mixture fluids

Combination	Purpose	Simulation method	Temperature	Pressure or density	References
CO_2+CH_4	VLE	GEMC	230 K	0.89-6.35 MPa	[105]
		AIMD	230 K	1-5.5 MPa	[161]
		GEMC	230 K	10.78-65.86 bar	[162]
		GEMC	250 K	14-80 bar	[163]
		NPT+test particle method	230-270 K	0.859-7.79 MPa	[164]
		GEMC	220 K	0-8 MPa	[165]
	Structural properties	MC	278-304 K	80-200 atm	[166]
		MD	323.15 K	238.14 kg/m^3	[167]
		GEMC	230 K	56 bar	[162]
	Thermodynamic properties	MD	323.15-573.15 K	19.94-99.93 MPa	[168]
		MD	510.72 K	100-1,000 kg/m^3	[169]
	Transport properties	MD	292.55-332.85 K	9-14.7 MPa	[170]
CO_2+CH_3OH	VLE	GEMC	333.15-353.15 K	0-15 MPa	[159]
		GEMC	290 K	1.379-4.826 MPa	[171]
	Structural properties	MD	323.15 K	9.952-16.96 MPa	[160]
		GEMC	313.15-324.9 K	10-40 MPa	[159]
		MD	293.15-338.15 K	10-20 MPa	[172]
		GEMC	290 K	2.758 MPa	[171]
		MD	313.2 K	10-16 MPa	[173]
	Thermodynamic properties	MD	323.15 K	9.952-16.96 MPa	[160]
		MD	304.2-328.1 K	8-30 MPa	[174]
		GEMC	313.15 K	10-20 MPa	[159]
		MC	60-150 °C	90-300 bar	[175]
		MD	363.15 K	70 MPa	[176]
	Transport properties	MD	310-350 K	15-30 MPa	[177]
		MD	313.2 K	10-16 MPa	[173]

Table 3. Continued

Combination	Purpose	Simulation method	Temperature	Pressure or density	References
CO_2+C_2H_6	VLE	NPT+test particle method	230-270 K	0.859-7.79 MPa	[164]
		GEMC	250 K	10-25 bar	[163]
		MD	223.15-283.15 K	0-6 MPa	[178]
	Transport properties	NEMD	150-280 K	880 kg/m^3	[179]
CO_2+C_2H_5OH	Structural properties	CPMD	318.5 K	699 kg/m^3	[180]
		MD	348 K	611 kg/m^3	[181]
		MD	293.15-338.15 K	5-25.5 MPa	[182]
		AIMD+MC	323 K	10 MPa	[183]
		MC	308-378 K	10-40 MPa	[184]
		MD	318.15 K	3.45-7.32 MPa	[185]
		MD	348 K	15.87 MPa	[186]
		MD	318.15 K	3.45-7.32 MPa	[187]
		MC	304-343 K	10 MPa	[188]
		MD	313.2 K	10-16 MPa	[173]
	VLE	MC	298.17-353.2 K	0-15 MPa	[183]
		MC	304-343 K	10 MPa	[188]
	Thermodynamic properties	MD	308.1-328.1 K	10-30 MPa	[174]
		MC	304-343 K	10 MPa	[188]
	Optical properties	MD	250-550 K	80 bar	[189]
	Transport properties	MD	313.2 K	10-16 MPa	[173]
CO_2+C_3H_6O (acetone)	Transport properties	MD	313.15 K	16 MPa	[190]
		MD	310-340 K	8-25 MPa	[191]
	Structural properties	MC	307.17-364.95 K	0.25-2[a]	[192]
	Thermodynamic properties	MC	1.01[b]	2[a]	[192]
		MD	308.1-328.1 K	10-30 MPa	[174]
CO_2+benzene (including benzene derivatives)	Transport properties	MD	313.15-333.15 K	1.35-2.1[a]	[193]
		MD	273.15-348.15 K	3.21-20.408 MPa	[194]
		MD	313.15 K	16 MPa	[195]
		MC	313-333 K	15 MPa	[196]
		MD	318.2-328.2 K	0-20 MPa	[170]
	Structural properties	AIMD			[193]
		MC	313-333 K	15 MPa	[196]
		MD	304-350 K	800 kg/m^3	[197]
	Thermodynamic properties	MC	308.15 K	7.8-30 MPa	[198]

[a] ρ/ρ_c, ρ_c is the critical density.
[b] T/T_c, T_c is the critical temperature.

both CO_2 [67,76] and methane [199,200], and their results of two models compared with those obtained by the GERG equation showed an overall derivation of 1% to 3% except for the Joule-Thomson coefficient. Skamoutous and Samios [167] used MD simulation to explore the local structure of S-CO_2-methane system by EPM2 and OPLS-AA [210] models for CO_2 and methane, respectively. Chatzis and Samios [160] performed molecular dynamics simulations of S-CO_2-methanol mixture system with methanol mole fraction in the range of 0.0939-0.1173 at 323.15 K and pressure of 9.952 to 16.76 MPa. They selected MSM, Exp-6, EPM, EPM2 for CO_2 [59,60,62,91] and J1, J2, H1, H2 for methanol. These models were tested and the EPM2 model of CO_2 and the J2 model of methanol were found to predict the PVT relationship of fluids in the region fairly well. Zhou et al. [194] carried out MD simulation of the diffusion coefficients of benzene and naphthalene in S-CO_2 by using spherical models and site-site models, respectively. Both models can accurately predict the self-diffusion coefficient. Their results show that although the spherical model is simple and the simulation time is short, its accuracy is poor. The site-site model, however, has high accuracy but needs a very long simulation time. Therefore, appropriate selection and collocation are important for molecular simulation to accurately predict the target property and improve efficiency.

In supercritical extraction, alcohols or acetone are usually added to S-CO_2 as co-solvents to improve the solubility and selectivity of S-CO_2 for providing better separation. Small amounts of co-solvents (e.g., 3 to 5 mol% of methanol or acetone) known as modifiers or entrainers, can be used to change the polarity and solvent strength of primary S-CO_2 [50]. However, when S-CO_2 is mixed with alcohols, there are local density inhomogeneity and aggregate formation, which are of interest to the researchers in S-CO_2 organic mixtures [159,160,174,181,183-187,201]. Chatzis and Samios [160] confirmed the presence of methanol aggregates in the S-CO_2 mixture fluids by the obtained structural and hydrogen bond data. Stubbs and Siepmann [159] studied the self-association of methanol in S-CO_2 at a series of temperatures and pressures close to the critical point of the mixture. They suggest that the origin of the solubility enhancement is likely to be the strong microscopic inhomogeneity of the solvent/entrainer structure as the alcohol entrainer forms hydrogen-bonded aggregates that efficiently solvate other polar molecules. Pressure has very little effect on aggregate formation, because although the increase in solvent density reduces the entropy loss of aggregation formation, it also makes S-CO_2 a better solvent, thus reducing the enthalpy of aggregate formation. Meanwhile, Stubbs et al. [159,202] proved that the interaction between co-solvent and solute molecules, especially the hydrogen bond between them, is the main driving force of polar solution. The increase of solubility parameters of S-CO_2 is the result of adding co-solvent with higher solubility. Skarmoutsos and Samios [201] calculated the effective local density, local density enhancement, and enhancement factor of S-CO_2 and supercritical methanol along the isotherm curve close to the critical temperature (T_r=1.03). The results showed that molecular polarity and hydrogen bond had a strong effect on the local density enhancement, and the local density enhancement value reached the maximum at the main phase density region near 0.7ρ_c. In calculation of solubility of S-CO_2-cosolvent system by Zhang et al. [174] (methanol, ethanol, acetone and cyclohexane), the solubility of S-CO_2-cosolvent system decreases with the increase of temperature, and increase of the increase of pressure, and linearly increases with the increase of density. This is because with the increase of pressure or the decrease of temperature, the intermolecular distance of CO_2 is shortened and the intermolecular interaction is enhanced, which leads to the improved solubility parameters of S-CO_2 solvent. In addition to the influence of temperature and pressure, the solubility parameters of S-CO_2 solvent can be adjusted and controlled by changing the entrainer concentration. In addition, by comparing the strength of co-solvent hydrogen bond and the influence of co-solvent on the solubility of S-CO_2, they concluded that there was a positive correlation between the strength of hydrogen bond and its influence on solubility. Yang et al. [185] showed that when pressure and temperature are fixed, the aggregate size of CO_2-organic liquid molecules and organic liquid - organic liquid molecules is affected by the structure, polarity and size. The dispersion coefficients of CO_2+hexane, CO_2+cyclohexane and CO_2+ethanol systems are affected by the aggregation degree and size of the aggregates formed by CO_2 and organic liquid and the pressure at fixed temperature. For S-CO_2-alcohol systems, the presence of hydrogen bonds is responsible for a variety of phenomena, such as the formation of aggregates, local density enhancement, and the effect on solubility. For infinite dilution solutions, alcohols almost do not have hydrogen bonds, and the hydrogen bond interaction between alcohols and CO_2 is weak [173].

In an infinite dilution solution, it is complicated and difficult to obtain the diffusion coefficient of supercritical system through experiments, but molecular simulation can solve this problem. Therefore, it is very common for molecular simulation to calculate the diffusion coefficient in infinite dilution [173,177,193,194,196,203]. Shi et al. [177] simulated the infinite dilution diffusion coefficient of methanol and ethanol in S-CO_2 by MD method, and they explained the reason for the influence of temperature and pressure on the diffusion coefficient: the diffusion coefficient increases with the increase of temperature. This is because with the increase of temperature, the thermal motion of molecules intensifies, and the influence of intermolecular forces weakens, which is advantageous to the molecular diffusion of solute molecules in CO_2, so that the diffusion coefficient of infinite dilution of solute molecules in S-CO_2 increases with the increase of temperature. The diffusion coefficient decreases with the increase of pressure, because with the increase of pressure, the density of the solution increases; the number of carbon dioxide molecules around the solute molecules increases and the spacing between molecules shrinks, which increases the intermolecular force and hinders the diffusion movement of solute molecules. So the diffusion coefficient of solute molecules decreases with the increase of pressure. Ferreira et al. [193] used AIMD method to study the atomic and molecular interactions of aromatic compounds in CO_2 and calculated the diffusion coefficients of benzene and toluene in S-CO_2; the results were also in good agreement with the experimental values. These studies show that molecular simulation is indeed a powerful tool for calculating diffusivity in infinite dilution solutions.

Understanding the phase behavior and critical properties of CO_2+solute in binary mixtures can facilitate the design and effective operation of supercritical extraction reactors. Phase equilibrium and critical property data provide guidance for system operation to avoid problems caused by binary mixtures of CO_2+solute, which are important for determining the tractability of these reactor materials [50]. Therefore, the application of molecular simulation to calculate the VLE properties of CO_2 organic mixtures also emerged rapidly (see Table 3), including the simulation in the non-critical region. Vrabec and Fischer [164] used NpT+test particle method to predict VLE property of methane+ethane, methane+carbon dioxide and carbon dioxide+ethane mixtures through molecular simulations in the early years of studying CO_2 mixture systems with molecular simulation. Later, Vrabec et al. [204] proposed a molecular model for 267 binary mixtures to simulate VLE by evaluating a large number of binary systems, and also confirmed the effectiveness of molecular simulation in predicting the properties of VLE. There are also many molecular simulations for various macromolecular systems of organics in S-CO_2 [205-207]. In addition to studying the mixture system of S-CO_2+simple organic molecules, it is one of the goals of molecular simulation to explore the mixture system of S-CO_2+derivatives of simple organic molecules such as fluorine [162,166,197] and alkyl [196] to replace hydrogen atom, and expand to more complex organic systems latter. More detail about complex organic solutes in S-CO_2 can be found in Stubbs's

review [21].

2. S-CO_2 Inorganic Mixture Fluids

In addition to supercritical extraction, which requires a certain understanding of the properties of S-CO_2 organic mixed fluid, mixing between CO_2 and inorganic matter is also crucial, no matter in critical or non-critical region, such as CO_2-H_2O system, as one of the most important geological fluids on the earth. An accurate understanding of the basic properties of the system is an important scientific issue, and can also provide theoretical guidance for the design of separation equipment in the chemical and energy industry. This part will illustrate the application of molecular simulation in several typical inorganic materials: water, ionic liquids (ILs), argon,

Table 4. An overview of molecular simulation in S-CO_2 inorganic mixture fluids

Combination	Purpose	Simulation method	Temperature	Pressure or density	References
CO_2+H_2O	VLE	GEMC	348-393 K	2.5-20.265 MPa	[208]
		MC	50-350 °C	0-100 MPa	[209]
		GEMC	298.15-348.15 K	100-400 bar	[81]
		GEMC	423-523 K	200-800 bar	[210]
		GEMC	323-523 K	200-800 bar	[83]
	Structural properties	AIMD	318.15 K	19 MPa	[211]
		AIMD	305.15 K	840-1,330 kg/m^3	[212]
		MC	313.15-473.15 K	300-900 kg/m^3	[213]
		MD	1.003, 1.26[b]	1.02-2.5[a]	[214]
		MD	1.003, 1.26[b]	0.3-2.5[a]	[215]
	Thermodynamic properties	MD	700-1,000 K	25 MPa	[103]
		MD	276 K	100-300 atm	[216]
	Transport properties	MD	283.15-623.15 K	0.1-100 MPa	[217]
		MD	298.15-523.15 K	5-100 MPa	[218]
		MD	323.15-1,023.15 K	200-1,000 MPa	[219]
		MD	1.003, 1.26[b]	1.02-2.5[a]	[214]
CO_2+ILs	Structural properties	AIMD	298 K		[220]
		MD	318.15 K	20 MPa	[221]
		MD	300 K		[222]
		AIMD	350 K		[223]
		MD	308.15 K	23 MPa	[224]
		MD	308.15 K	23 MPa	[225]
	Thermodynamic properties	MD	313.15 K		[226]
		MD	300 K		[222]
		MD	35-45 °C		[227]
	Transport properties	MD	313.15 K	0.1-10 MPa	[226]
		MD	300 K		[222]
CO_2+Ar	Thermodynamic properties	MC	248-288.15 K	0-14 MPa	[228]
		MD	510.72 K	100-1,000 kg/m^3	[169]
		GEMC	273.26-323.18 K		[229]
CO_2+Nitrogen/ Nitrogen oxides	VLE	MC	300-330 K	0-10 MPa	[230]
		MC	253.15-273.15 K	2.25-11.48 MPa	[231]
		MD	218.15-253.15 K	0-16 MPa	[230]
	Thermodynamic properties	MC	200-500 K	1 MPa	[230]
		QMD	500-8,000 K	1,800-3,400 kg/m^3	[232]
		GEMC	273.15-320 K		[229]
		MC	220-273.15 K	0-20 MPa	[228]
		MD	677-977 K	10-20 MPa	[233]
	Transport properties	MD	263.15-273.15 K	2-8 MPa	[231]
CO_2+Xe	Thermodynamic properties	MD	677-977 K	15-20 MPa	[233]
	Transport properties	MD	373-873 K	8-20 MPa	[234]

[a] ρ/ρ_c, ρ_c is the critical density.
[b] T/T_c, T_c is the critical temperature.

xenon, nitrogen and its nitrogen oxides. Table 4 summarizes and consolidates the literature by composition, thermodynamic range, and purpose of simulation, and includes a small number of simulations in non-critical regions as a supplement.

As one of the most frequently studied objects of molecular simulation, water has developed many potential energy models like CO_2, such as SPC, SPC/E, TIP4P, TIP4P/2005, etc. [21]. However, a question arises: how to select and match the models of S-CO_2-H_2O system to accurately predict the system properties? Vorholz et al. [208] used GEMC method to predict the VLE properties of CO_2-H_2O in the temperature range of 348-393 K. EPM2, SPC and TIP4P were used for CO_2 and H_2O models, respectively. Their results agree well with the experimental data, but the differences are still greater than the experimental uncertainties of most properties. Liu et al. [209] compared five CO_2-H_2O system model combinations used to predict phase behavior in a wide range of pressure and temperature: EPM2-TIP4P/2005, EPM2-TIP4P, EPM2-SPC, TraPPE-TIP4P/2005 and Exp-6-Exp-6. The results show that Exp-6-Exp-6 is the best model to predict the vapor phase composition in the range of T≤250 °C, and TraPPE-TIP4P2005 is the most consistent with the experiment values at the liquid sides. Within the range of T>250 °C, only the Exp-6-Exp-6 can qualitatively predict the existence of critical point. However, the combination of these nonpolarizable models still has a large global deviation in predicting phase equilibrium composition, which is particularly severe in CO_2-rich region. Vlcek et al. [81] optimized the unlike-pair interaction of SPC/E-EPM2 combination by taking the overpolarization of the SPC/E water molecule into account. The optimized combination showed a great improvement in phase equilibrium composition, but there is still a deviation at 348.15 K. Orozco et al. [210] described the phase equilibrium composition by optimizing the across interaction parameters of nonpolarizable models between water and CO_2. Their results showed that the optimized SPC/E-TraPPE combinations was not satisfactory in predicting phase equilibrium composition, concluding that the existing LJ-based fixed-point-charge models had great accuracy limitation for describing the phase behavior of water/CO_2 mixture system. Jiang et al. [83] optimized the combination consisting of three water polarization models (BK3, GCP and HBP) and one CO_2 polarization model (PGC) to represent water/CO_2 mixture. They found that the combination of BK3, GCP and PGC models optimized to the experimental phase composition data still underestimated the solubility of water in CO_2-rich region. But there was a slight improvement over the nonpolarizable model. For the combination of HBP model, which can clearly showed the hydrogen bond between water and CO_2 and PGC model, the phase equilibrium composition can be well predicted in both water- and CO_2-rich phases simultaneously. It can be seen that for water-CO_2 system, the LJ-based fixed-point-charge models can no longer meet the requirements of describing phase behavior, and more realistic physical interactions, such as the effect of polarizability, need to be introduced. What is more, it has proven to be effective in optimizing the phase behavior of the mixed system by considering the effect of polarizability in the cross interaction [81,83].

Thermodynamic and transport properties of water/CO_2 mixtures have also been studied by molecular simulation. Yang et al. [103] calculated the thermodynamic properties of water/CO_2 mixture system using TIP4P-TraPPE-flex combination by MD simulation and compared it with PR-EOS. They found that MD simulation and PR-EOS had similar accuracy in calculating heat capacity. However, the accuracy of PR-EOS is much poorer when the CO_2 mole faction is relatively small and the temperature is below 800 K. Moultos et al. [217-219] calculated the diffusion coefficient of water/CO_2 mixture system using a variety of model combinations over a wide range of temperature and pressure through MD simulation, and their results showed that the cross interactions between water and CO_2 have less effect on calculating diffusion coefficient.

Hydrogen-bonded compounds can form aggregates in SCFs, so the existence of aggregates in CO_2-H_2O system is not surprising. Tafazzolo and Khanlarhani [213] studied the association degree of water in S-CO_2 at a wide density and temperature by testing particle insertion technology. The results showed that the association constant of water decreased with temperature and was weakly dependent on CO_2 concentration. It is proved that moderate CO_2-H_2O compounds will not substantially interfere with the hydrogen bond of water molecules. Glezakou et al. [211] analyzed the radial and orientation distribution function of intermolecular interaction in the CO_2-H_2O system, and showed that the presence of water molecules would not interfere with the optimal configuration of T-shaped CO_2 molecules. They also observed the formation of water aggregates due to the strong enthalpy of hydrogen bonds between water. Although there is some interaction between CO_2 and water molecules, it is not enough to break the solvated water cluster. ILs, as another green solvent, have made some progress in reaction and separation applications. Extracting organic matter from ILs with S-CO_2 and studying the properties of S-CO_2-ILs system are the future development direction of green chemistry [226]. Ionic liquid [bmim][PF6] mixed with S-CO_2 as the typical representative of the S-CO_2-ILs system, is one of the objects of the researches interested in [220-222,224-226]. S-CO_2-ILs system is very different from S-CO_2 organic mixture fluid. In S-CO_2 organic mixture fluid, S-CO_2 is often used as a solvent, but in S-CO_2-ILs system, S-CO_2 is treated as solute because ILs can dissolve S-CO_2 and S-CO_2 cannot dissolve ILs [226]. The diffusion coefficient of S-CO_2-ILs system is much smaller than that of S-CO_2 organic fluids mixing with methanol and ethanol, and the viscosity decreases significantly [226]. When S-CO_2 is dissolved in ILs, its partial molar volume is much smaller than that observed in most other solvents. Huang et al. [221] explained this phenomenon as: CO_2 occupies preexisting interstitial space in ILs and then reorganizes to accommodate CO_2, which rationalizes a negligible increase in the molar volume of the mixture compared to pure ILs. In recent years, Zhu et al. [224-225] also carried out detailed studies on the microstructure and thermodynamic behavior of S-CO_2 microemulsions containing ILs.

S-CO_2 and gas mixtures are another focus of research, especially in the field of carbon capture and storage (CCS). Impurities in the CCS chain can greatly affect the physical properties of CO_2, which has important implications for the design of CO_2 compression, transport, storage, safety and cost. Therefore, there is an urgent need to understand and predict the properties of impure carbon dioxide (containing impurities such as N_2, O_2, H_2) to assist CCS imple-

mentation [229]. The related literatures of S-CO_2 and typical gas mixture system are listed in Table 4. Note that the mixing system between CO_2 and NO_2 is complex, because nitrogen dioxide exists as a mixture of monomer (NO_2) and dimer (N_2O_4) under certain pressure and temperature conditions. The composition of NO_2-N_2O_4 equilibrium mixture depends on pressure and temperature conditions and dimer are advantageous at higher pressure and low temperature [230]. In addition to the conventional thermodynamic range, CO_2-nitrogen/nitrogen oxides system are more complex under extreme conditions [232]. To the author's knowledge, only a few literatures are listed in Table 4 on the study of mixed system of S-CO_2 with inert gases Ar and Xe. In several recent papers, it is a new idea to try to improve the performance of the S-CO_2 Bryton cycle by adding inert gas Xe. Du and colleagues [233,234] investigated the effects of adding Xe on the viscosity and isobaric heat capacity of S-CO_2 system by MD simulation. The results showed that when adding Xe to S-CO_2 systems, the viscosity coefficient will have a great relative change, which may not be conducive to the S-CO_2 Bryton cycle, and the isobaric heat capacity decreased continuously, more obviously than N_2.

3. S-CO_2 Multicomponent Mixture Fluids

The applications of molecular simulation in CO_2 multicomponent mixture (mostly ternary mixtures) have been studied in the same early stage as binary mixtures, but these studies are often not extended to the supercritical region [163,178]. However, in recent years, people have begun to pay more and more attention to the application of S-CO_2 multicomponent mixture molecular simulation in the fields of petroleum, natural gas, chemical industry, CCS, supercritical water gasification and power generation. To enhance the physical understanding and theoretical modelling of complex S-CO_2 compounds or due to the lack of experimental data in supercritical region, researchers have focused on the phase behavior of natural gas hydrates [235-237], the surface interface properties of crude oil and water [238-242], optimization of S-CO_2 Bryton cycle [243], reverse formation in S-CO_2 [244,245], S-CO_2 multicomponent containing ILs [241], effect of hydrogen bond on aggregate in S-CO_2 [183], transport properties of S-CO_2-acetone-H_2O system [247] and thermodynamic and transport properties of supercritical water gasification of coal [248-251].

It is important to note that tends to be an important component of the S-CO_2 multicomponent mixture, because the original fuel like natural gas contains water and CO_2 under the original storage conditions. Understanding the properties of the multicomponent mixture of water system containing CO_2 for sequestration, enhanced oil recovery (EOR) and purification is important [237, 242]. Take the molecular simulation of S-CO_2 multicomponent mixtures in terms of EOR as an example. In practice, the composition of crude oil is very complex, including alkanes, cycloalkanes, aromatic hydrocarbons, alkenes, and a small amount of sulfur, nitrogen and other impurities. For molecular simulation in EOR, appropriate simplification will be carried out, that is, a small amount of impurity elements will be ignored, and various organic components will be simplified into one or two components through appropriate chemical calculation as prototype oil, such as decane [239,242], hexane [238,240], octane, benzene, xylene [240], benzene+hexane, benzene+octane, xylene+hexane and xylene+octane [241]. Liu et al. [239] used MD simulation to study the effect of S-CO_2 on the water-oil interface. Their results showed that the interfacial tension (IFT) of S-CO_2-H_2O-decane system decreased linearly with the increase of S-CO_2 mole fraction, and the interaction between CO_2-water and CO_2-decane was large but the difference between the two interactions was small. When the difference is small enough, the addition of S-CO_2 will reduce the IFT of water-oil system and enhance the transport performance of water-oil system, which is beneficial to improving the oil recovery rate. Mohammed and Mansoori then used pure hydrocarbon [240] and binary hydrocarbon [241] as prototype oil, respectively, to study the effect of the addition of S-CO_2 on the interface properties of water-oil system. Their results show that S-CO_2 accumulates at the interface and reduces the IFT of the water-oil system. As the mole fraction increases, the diffusion coefficient of the hydrocarbon increases, which is determined by the molecular weight and polarity of the hydrocarbon [240]. In the simulation study using binary hydrocarbon as prototype oil [241], they confirmed the conclusion that the two decisive factors of the increase of diffusion coefficient with the addition of S-CO_2 are molecular weight and polarity of hydrocarbon by adding asphaltenes.

Supercritical water gasification is a kind of clean fuel utilization technology, the technology of important products of H_2O/H_2/CO_2 ternary mixtures in supercritical thermal physical properties, the data of which are still lacking, needing people to fill the gap. However, harsh experimental conditions force people to find new ways, and molecular simulation has become a powerful alternative. In recent years, Yang and his colleagues [248-251] have conducted a series of studies on the thermodynamic and transport properties of H_2O/H_2/CO_2 ternary mixture in supercritical region using MD simulations, including obtaining their PVT properties [248,251], viscosity and self-diffusion coefficient [249], and thermal conductivity [250]. Notably, in addition to calculating the target properties of the H_2O/H_2/CO_2 ternary mixture, they also studied the effect of system size [248,250]. When calculating the PVT properties, their study showed that the uncertainty decreases with the increase of the system size, but this effect appears to be marginal, and it can be neglected that the initial spatial distribution of molecules affected the results obtained by MD simulation [248]. When calculating thermal conductivity, they conducted simulations of different system sizes, and the results showed that the EMD method used to calculate thermal conductivity from their system was actually insensitive to the system size [250]. These results can provide appropriate guidance to the efficiency of molecular simulations.

SUMMARY AND FUTURE WORK

Molecular simulation, as a powerful computer simulation technique, has been widely used in S-CO_2 pure and mixture fluids. Because of its low cost and high efficiency, it can effectively replace expensive and complex experiments. From what has been reviewed, we can draw the following conclusions:

1. The quality of force field model is the key to determining the "realism" of molecular simulation, so it is particularly important to choose an appropriate force field to calculate target properties.

2. The force field model for CO_2 now is rich [21], but these mod-

els are still only applicable to specific properties calculation under the premise of ensuring accuracy. At present, no general model is suitable for the calculation of all properties. Although Zhang's model [20] has achieved good global accuracy, there are still large deviations in calculating some properties such as thermal conductivity.

3. The rigid three-site model is generally more accurate than other models, such as the flexible three-site model or the single-site model. Although CO_2 molecules have been found to change from linear to non-linear in the supercritical region, the effect of this change is marginal.

4. The calculation accuracy of NEMD is higher than that of EMD when calculating transport properties, but NEMD is cumbersome when calculating multiple transport properties, because each transport property needs to be simulated separately. The EMD is less precise but more efficient, because it can simultaneously calculate multiple transport properties for a specific fluid. Meanwhile, if the model is accurate enough, EMD can also achieve the accuracy of NEMD.

5. In the supercritical region, T-shaped geometry dominates the configuration of CO_2 nearest neighbor molecular structure. In the first coordination shell, T-shaped geometry has the same convexity and domination. This preference disappears rapidly with the increase of distance.

6. Molecular simulation studies on S-CO_2 multicomponent mixtures have emerged in recent years. These studies are mainly applied to the industry of petroleum, natural gas, CCS and supercritical water gasification technology, etc. Most of them focus on ternary mixtures, and there are a few studies on mixtures with more components. It is one of the development directions of the later molecular simulation towards the more complex mixture of S-CO_2.

Recently, similar to the liquid to gas boiling phenomenon in the subcritical region, pseudo-boiling, which occurs when SCF crosses the Widom line (an extension of vapor-liquid coexistence), has become a hot topic in the field of SCF. In 2015, Banuti [252] proved the existence of pseudo-boiling phenomenon by theoretical analysis, and gave the pseudo-boiling curve of vapor-liquid coexistence in the supercritical region. Later, many researchers studied the pseudo-boiling phenomenon of different fluids [253]. Therefore, we will use molecular simulation to study the pseudo-boiling of S-CO_2 in the future.

ACKNOWLEDGEMENTS

The authors gratefully acknowledge the support by the National Natural Science Foundation of China (Grant No. 52106087) and the Fundamental Research Funds for the Central Universities of China (Grant No. 531118010211).

CONFLICT OF INTEREST

The authors declare that they have no conflict of interest regarding the publication of this paper.

SUPPORTING INFORMATION

Additional information as noted in the text. This information is available via the Internet at http://www.springer.com/chemistry/journal/11814.

REFERENCES

1. B. J. Alder and T. E. Wainwright, *J. Chem. Phys.*, **27**, 1208 (1957).
2. B. J. Alder and T. E. Wainwright, *J. Chem. Phys.*, **31**, 459 (1959).
3. A. Rahman, *Phys. Rev.*, **136**, A405 (1964).
4. A. Singh, V. Orsat and V. Raghavan, *Biomolecules*, **3**, 168 (2013).
5. A. Singh, S. K. Vanga, V. Orsat and V. Raghavan, *Crit. Rev. Food Sci. Nutr.*, **58**, 2779 (2018).
6. W. F. de Azevedo Jr., *Curr. Med. Chem.*, **18**, 1353 (2011).
7. N. Todorova, F. S. Legge, H. Treutlein and I. Yarovsky, *J. Phys. Chem. B*, **112**, 11137 (2008).
8. R. Komanduri and L. M. Raff, *Proc. Inst. Mech. Eng. Part B-J. Eng. Manuf.*, **215**, 1639 (2001).
9. S. Goel, X. C. Luo, A. Agrawal and R. L. Reuben, *Int. J. Mach. Tools Manuf.*, **88**, 131 (2015).
10. Y. L. Dong, Q. Y. Li and A. Martini, *J. Vac. Sci. Technol. A-Vac. Surf. Films*, **31**, 030801 (2013).
11. Z. Y. Ma, R. P. Gamage, T. Rathnaweera and L. Kong, *Appl. Clay Sci.*, **168**, 436 (2019).
12. Y. Qin, X. N. Yang, Y. F. Zhu and J. L. Ping, *J. Phys. Chem. C*, **112**, 12815 (2008).
13. L. L. Zhao, S. C. Lin, J. D. Mendenhall, P. K. Yuet and D. Blankschtein, *J. Phys. Chem. B*, **115**, 6076 (2011).
14. X. D. Zhang and D. A. Drabold, *Phys. Rev. Lett.*, **83**, 5042 (1999).
15. A. S. Rogachev, S. G. Vadchenko, F. Baras, O. Politano, S. Rouvimov, N. V. Sachkova, M. D. Grapes, T. P. Weihs and A. S. Mukasyan, *Combust. Flame*, **166**, 158 (2016).
16. S. M. Fatemi and M. Foroutan, *J. Iran. Chem. Soc.*, **14**, 269 (2017).
17. J. J. Lao, M. N. Tam, D. Pinisetty and N. Gupta, *JOM*, **65**, 245 (2016).
18. B. Mantisi, *Comput. Mater. Sci.*, **118**, 245 (2016).
19. Q. H. Wei, Y. F. Zhang, Y. N. Wang and M. M. Yang, *J. Mater. Sci.*, **52**, 12889 (2017).
20. Z. G. Zhang and Z. H. Duan, *J. Chem. Phys.*, **122**, 214507 (2005).
21. J. M. Stubbs, *J. Supercrit. Fluids*, **108**, 104 (2016).
22. F. J. G. Ortiz and A. Kruse, *React. Chem. Eng.*, **5**, 424 (2020).
23. Z. Knez, E. Markocic, M. Leitgeb, M. Primozic, M. K. Hrncic and M. Skerget, *Energy*, **77**, 235 (2014).
24. W.-C. Tsai and Y. D. Wang, *Prog. Polym. Sci.*, **98**, 101161 (2019).
25. G. L. Liao, L. J. Liu, J. Q. E, F. Zhang, J. W. Chen, Y. W. Deng and H. Zhu, *Engergy Conv. Manag.*, **199**, 111986 (2019).
26. R. Davarnejad, K. M. Kassim, A. Zainal and S. A. Sata, *J. Food Eng.*, **89**, 472 (2008).
27. C. Perakis, V. Louli, E. Voutsas and K. Magoulas, *J. Supercrit. Fluids*, **55**, 573 (2010).
28. T. T. Wu, Q. Z. Xue, X. F. Li, Y. H. Tao, Y. K. Jin, C. C. Ling, and S. F. Lu, *J. Supercrit. Fluids*, **107**, 499 (2016).
29. T. M. Fang, J. Q. Shi, X. L. Sun, Y. Shen, Y. G. Yan, J. Zhang and B. Liu, *J. Supercrit. Fluids*, **113**, 10 (2016).
30. A. Baiker and R. Wandeler, *CATTECH*, **4**, 128 (2000).
31. Y. Zhang, J. C. Yang, Y. X. Yu and Y. G. Li, *Prog. Chem.*, **17**, 955 (2005).
32. H. Luo, R. Wang, W. Y. Fan, Z. M. Li, T. Ma and G. Z. Nan, *Acta Petrolei Sinica (Petroleum Processing Section)*, **31**, 78 (2015).

33. L. B. Koppel and J. M. Smith, *J. Chem. Eng. Data*, **5**, 437 (1960).
34. J. W. Magee and J. F. Ely, *Int. J. Thermophys.*, **7**, 1163 (1986).
35. L. Beck, G. Ernst and J. Gurtner, *J. Chem. Thermodyn.*, **34**, 277 (2002).
36. L. Dordain, J.-Y. Coxam, J. R. Quit, E. W. Lemmon and S. G. Penoncello, *J. Supercrit. Fluids*, **8**, 228 (1995).
37. J. R. Boulton and F. P. Stein, *Fluid Phase Equilib.*, **91**, 159 (1993).
38. R. Hasse and W. Tillmann, *Zeitschrift für Physikalische Chemie*, **186**, 99 (1994).
39. X. F. Zhang, X. G. Zhang, B. X. Han, L. Shi, H. P. Li and G. Y. Yang, *J. Supercrit. Fluids*, **24**, 193 (2002).
40. A. F. Estrada-Alexanders and J. P. M. Trusler, *J. Chem. Thermodyn.*, **30**, 1589 (1998).
41. Q. Liu, X. J. Feng, B. L. An and Y. Y. Duan, *J. Chem. Eng. Data*, **59**, 2788 (2014).
42. A. Michels, J. V. Sengers and P. S. Van der Gulik, *Physica*, **28**, 1216 (1962).
43. B. Leneinder, R. Tufeu, P. Bury and J. V. Sengers, *Berichte der Bunsengesellschaft für physikalische Chemie*, **77**, 262 (1973).
44. V. Vesovic, W. A. Wakeham, G. A. Olchowy, J. V. Segners, J. T. R. Watson and J. Millat, *J. Phys. Chem. Ref. Data*, **19**, 763 (1990).
45. J. Kestin, H. E. Khalifa and W. A. Wakeham, *J. Chem. Phys.*, **65**, 5186 (1976).
46. I. N. Hunter, G. Marsh, G. P. Matthews and E. B. Smith, *Int. J. Thermophys.*, **14**, 819 (1993).
47. A. F. Estrada-Alexanders and J. J. Hurly, *J. Chem. Thermodyn.*, **40**, 193 (2008).
48. A. Laesecke and C. D. Muzny, *J. Phys. Chem. Ref. Data*, **46**, 013107 (2017).
49. M. L. Huber, E. A. Sykioti, M. J. Assal and R. A. Perkins, *J. Phys. Chem. Ref. Data*, **45**, 013102 (2016).
50. P. Nikolai, B. Rabiyat, A. Aslan and A. Ilmutdin, *J. Therm. Sci.*, **28**, 394 (2019).
51. J. Kolafa, I. Nezbeda and M. Lisal, *Mol. Phys.*, **99**, 1751 (2001).
52. J. P. Bouanich, *J. Quant. Spectrosc. Radiat. Transf.*, **47**, 243 (1992).
53. H. Higashi, Y. Iwai, H. Uchida and Y. Arai, *J. Supercrit. Fluids*, **13**, 93 (1998).
54. W. A. Steele and H. A. Posch, *J. Chem. Soc., Faraday Trans. 2*, **83**, 1843 (1987).
55. M. I. H. Panhuis, C. H. Patterson and R. M. Lynden-Bell, *Mol. Phys.*, **94**, 963 (1998).
56. M. E. Tuckerman and W. Langel, *J. Chem. Phys.*, **100**, 6368 (1994).
57. A. M. Zhu, X. B. Zhang, Q. L. Liu and Q. G. Zhang, *Chin. J. Chem. Eng.*, **17**, 268 (2009).
58. L. M. Yan and S. M. Zhu, *Theory and practice of molecular dynamics simulation*, Science Press, Beijing (2013).
59. C. S. Murthy, K. Singer and I. R. McDonald, *Mol. Phys.*, **44**, 135 (1981).
60. C. S. Murthy, S. F. O'Shea and I. R. McDonald, *Mol. Phys.*, **50**, 531 (1983).
61. L. C. Geiger, B. M. Ladanvi and M. E. Chapin, *J. Chem. Phys.*, **93**, 4533 (1990).
62. J. G. Harris and K. H. Yung, *J. Phys. Chem.*, **99**, 12021 (1995).
63. B. J. Palmer and B. C. Garrett, *J. Chem. Phys.*, **98**, 4047 (1993).
64. S. B. Zhu and G. W. Robinson, *Comput. Phys. Commun.*, **52**, 317 (1989).
65. T. Merker, J. Vrabec and H. Hasse, *J. Chem. Phys.*, **129**, 214507 (2008).
66. Z. G. Zhang and Z. H. Duan, *J. Chem. Phys.*, **129**, 087101 (2008).
67. J. J. Potoff and J. I. Siepmann, *AIChE J.*, **47**, 1676 (2001).
68. D. Moller and J. Fischer, *Fluid Phase Equilib.*, **100**, 35 (1994).
69. J. Vrabec, J. Stoll and H. Hasse, *J. Phys. Chem. B*, **105**, 12126 (2001).
70. T. Merker, C. Engin, J. Vrabec and H. Hasse, *J. Chem. Phys.*, **132**, 234512 (2010).
71. C. Nieto-Draghi, T. de Bruin, J. Perez-Pellitero, J. B. Avalos and A. D. Mackie, *J. Chem. Phys.*, **126**, 064509 (2007).
72. M. E. Perez-Blanco and E. J. Maginn, *J. Phys. Chem. B*, **114**, 11827 (2010).
73. R. T. Cygan, V. N. Romanov and E. M. Myshakin, *J. Phys. Chem C*, **116**, 13079 (2012).
74. Y. Zhang, J. C. Yang and Y. X. Yu, *J. Phys. Chem. B*, **109**, 13375 (2005).
75. K. E. Anderson, S. L. Mielke, J. I. Siepmann and D. G. Truhlar, *J. Phys. Chem A*, **113**, 2053 (2009).
76. C. Avendano, T. Lafitte, A. Galindo, C. S. Adjiman, G. Jackson and E. A. Muller, *J. Phys. Chem. B*, **115**, 11154 (2011).
77. T. G. Gibbons and M. L. Klein, *J. Chem. Phys.*, **60**, 112 (1974).
78. J. D. Johnson and M. S. Shaw, *J. Chem. Phys.*, **83**, 1271 (1985).
79. A. Chacin, J. M. Vazquez and E. A. Muller, *Fluid Phase Equilib.*, **165**, 147 (1999).
80. R. A. X. Persson, *J. Chem. Phys.*, **134**, 034312 (2011).
81. L. Vlcek, A. A. Chialvo and D. R. Cole, *J. Phys. Chem. B*, **115**, 8775 (2011).
82. F. F. Wang, R. Kumar and K. D. Jordan, *Theor. Chem. Acc.*, **131**, 1 (2012).
83. H. Jiang, I. G. Economou and A. Z. Panagiotopoulos, *J. Phys. Chem. B*, **121**, 1386 (2017).
84. K. Heijmans, I. C. Tranca, D. M. J. Smeulders, T. J. H. Vlugt and S. V. Gaastra-Nedea, *J. Chem. Theory Comput.*, **17**, 322 (2021).
85. K. B. Domanski, O. Kitao and K. Nakanishi, *Mol. Simul.*, **12**, 343 (1994).
86. G. Steinebrunner, A. J. Dyson, B. Kirchner and H. Huber, *J. Chem. Phys.*, **109**, 3153 (1998).
87. R. Bukowski, J. Sadlej, B. Jeziorski, P. Jankowski, K. Szalewicz, S. A. Kucharsaki, H. L. Williams and B. M. Rice, *J. Chem. Phys.*, **110**, 3785 (1999).
88. S. Bock, E. Bich and E. Vogel, *Chem. Phys.*, **257**, 147 (2000).
89. J. W. Shen, O. Kitao and K. Nakanishi, *Fluid Phase Equilib.*, **120**, 81 (1996).
90. S. Tsuzuki, T. Uchimaru, M. Mikami and K. Tanabe, *Chem. Phys. Lett.*, **252**, 206 (1996).
91. S. Tsuzuki and K. Tanabe, *Comput. Mater. Sci.*, **14**, 220 (1999).
92. K. Kobashi and T. Kihara, *J. Chem. Phys.*, **72**, 3216 (1980).
93. C. M. Destrigneville and J. P. Brodholt, *Chem. Geol.*, **133**, 53 (1996).
94. B. M. Mognetti, M. Oettel, P. Virnau, L. Yelash and K. Binder, *Mol. Phys.*, **107**, 331 (2009).
95. H. J. Bohm, C. Meissner and R. Ahlrichs, *Mol. Phys.*, **53**, 651 (1984).
96. R. D. Etters and B. Kuchta, *J. Chem. Phys.*, **90**, 4537 (1989).
97. G. Perez-Sanchez, D. Gonzale-Salgado, M. M. Pineiro and C. Vega, *J. Chem. Phys.*, **138**, 084506 (2013).
98. C. G. Aimoli, E. J. Maginn and C. R. A. Abreu, *Fluid Phase Equilib.*, **368**, 80 (2014).
99. C. G. Aimoli, E. J. Maginn and C. R. A. Abreu, *J. Chem. Phys.*, **141**,

134101 (2014).
100. M. Lagache, P. Ungerer, A. Boutin and A. H. Fuchs, *Phys. Chem. Chem. Phys.*, **3**, 4333 (2001).
101. M. H. Lagache, P. Ungerer and A. Boutin, *Fluid Phase Equilib.*, **220**, 211 (2004).
102. C. M. Colina, C. G. Olivera-Fuentes, F. R. Siperstein, M. Lisal and K. E. Gubbins, *Mol. Simul.*, **29**, 405 (2003).
103. X. M. Yang, Y. Y. Feng, J. H. Jin, Y. B. Liu and B. Y. Cao, *J. Mol. Liq.*, **299**, 112133 (2020).
104. R. Span and W. Wagner, *J. Phys. Chem. Ref. Data*, **25**, 1509 (1996).
105. Z. Yang, M. Q. Gong, Y. Zhou, X. Q. Dong, X. D. Li, H. Y. Li and J. F. Wu, *Sci. China Tech. Sci.*, **58**, 650 (2015).
106. D. Y. Peng and D. B. Robinson, *Ind. Eng. Chem. Fundam.*, **15**, 59 (1976).
107. L. Chen, S. Y. Wang and W. Q. Tao, *Energy*, **179**, 1094 (2019).
108. P. Ungerer, C. Nieto-Draghi, B. Rousseau, G. Ahunbay and V. Lachet, *J. Mol. Liq.*, **134**, 71 (2007).
109. M. S. Green, *J. Chem. Phys.*, **22**, 398 (1954).
110. R. Kubo, *J. Phys. Soc. Jpn.*, **12**, 570 (1957).
111. A. Kinaci, J. B. Haskins and T. Cagin, *J. Chem. Phys.*, **137**, 014106 (2012).
112. A. Tenenbaum, G. Ciccotti and R. Gallico, *Phys. Rev. A*, **25**, 2778 (1982).
113. D. R. Wheeler, N. G. Fuller and R. L. Rowley, *Mol. Phys.*, **92**, 55 (1997).
114. F. Muller-Plathe, *J. Chem. Phys.*, **106**, 6082 (1997).
115. T. Ikeshoji and B. Hafskjold, *Mol. Phys.*, **81**, 251 (1994).
116. P. Jund and R. Jullien, *Phys. Rev. B*, **59**, 13707 (1999).
117. G. Galliero, C. Boned, A. Baylaucq and F. Montel, *Fluid Phase Equilib.*, **234**, 56 (2005).
118. H. M. Zhong, S. H. Lai, J. Y. Wang, W. D. Qiu, H.-D. Ludemann and L. P. Chen, *J. Chem. Eng. Data*, **60**, 2188 (2015).
119. B. J. Parmer, *Phys. Rev. E*, **49**, 359 (1994).
120. B. Hess, *J. Chem. Phys.*, **116**, 209 (2002).
121. Y. Y. Wang, Z. J. Zhao, Y. F. Liu, D. J. Wang, C. Ma and J. P. Liu, *Energy*, **176**, 103 (2019).
122. G. H. Tang, C. Bi, Y. Zhao and W. Q. Tao, *Energy*, **90**, 701 (2015).
123. M. O. Onvekonwu, *Energy*, **13**, 619 (1988).
124. P. E. Hopkins, B. Kaehr, E. S. Piekos, D. Dunphy and C. J. Brinker, *J. Appl. Phys.*, **111**, 113532 (2012).
125. T. Groß, J. Buchhauser and H. D. Ludemann, *J. Chem. Phys.*, **109**, 4518 (1998).
126. Y. He, M. H. Zhang and H. X. Jiang, *Chem. Ind. Eng.*, **26**, 57 (2009).
127. H. Sun, P. Ren and J. R. Fried, *Comput. Theor. Polym. Sci.*, **8**, 229 (1998).
128. H. Sun, *J. Phys. Chem. B*, **102**, 7338 (1998).
129. H. Higashi and K. Tamura, *Mol. Simul.*, **36**, 772 (2010).
130. I. Shvab and R. J. Sadus, *J. Chem. Phys.*, **140**, 104505 (2014).
131. M. Saharay and S. Balasubramanian, *J. Phys. Chem. B*, **111**, 387 (2007).
132. M. Saharay and S. Balasubramanian, *J. Chem. Phys.*, **120**, 9694 (2004).
133. S. Balasubramanian, A. Kohlmever and M. L. Klein, *J. Chem. Phys.*, **131**, 144506 (2009).
134. T. A. Steriotis, K. L. Stefanopoulos, A. C. Mitropoulos, N. K. Kanellopoulos, A. Hoser and M. Hofmann, *Appl. Phys. A*, **74**, S1333 (2002).
135. A. K. Adya and C. J. Wormald, *Mol. Phys.*, **74**, 735 (1991).
136. S. Chiappini, *Mol. Phys.*, **89**, 975 (1996).
137. P. Cipriani, M. Nardone and F. P. Ricci, *Physica B*, **241**, 940 (1997).
138. P. Cipriani, M. Nardone, F. P. Ricci and M. A. Ricci, *Mol. Phys.*, **99**, 301 (2001).
139. J. B. Van Tricht, H. Fredrikze and J. Van der Laan, *Mol. Phys.*, **52**, 115 (1984).
140. R. Ishii, S. Okazaki, I. Okada, M. Furusaka, N. Watanabe, M. Misawa and T. Fukunaga, *Chem. Phys. Lett.*, **240**, 84 (1995).
141. R. Ishii, S. Okazaki, I. Okada, M. Furusaka, N. Watanabe, M. Misawa and T. Fukunaga, *J. Chem. Phys.*, **105**, 7011 (1996).
142. K. Nishikawa and M. Takematsu, *Chem. Phys. Lett.*, **226**, 359 (1994).
143. L. Temleitner and L. Pusztai, *J. Phys.-Condes. Matter*, **19**, 335203 (2007).
144. T. Sato, M. Sugiyama, K. Itoh, K. Mori, T. Fukunaga, M. Misawa, T. Otomo and S. Takata, *Phys. Rev. E*, **78**, 051503 (2008).
145. T. Sato, M. Sugiyama, M. Misawa, S. Takata, T. Otomo, K. Itoh, K. Mori and T. Fukunaga, *J. Phys.-Condes. Matter*, **20**, 104203 (2008).
146. M. Saharay and S. Balasubramanian, *ChemPhysChem*, **5**, 1442 (2004).
147. V. V. Brazhkin, Y. D. Fomin, A. G. Lyapin, V. N. Ryzhov and K. Trachenko, *Phys. Rev. E*, **85**, 031203 (2012).
148. D. Bolmatov, V. V. Brazhkin, Y. D. Fomin, V. N. Ryzhov and K. Trachenko, *J. Chem. Phys.*, **139**, 234501 (2013).
149. D. Bolmatov, D. Zay'yalov, M. Gao and M. Zhernenkov, *J. Phys. Chem. Lett.*, **5**, 2785 (2014).
150. C. Yang, V. V. Brazhkin, M. T. Dove and K. Trachenko, *Phys. Rev. E*, **91**, 012112 (2015).
151. C. J. Cockrell, O. Dicks, L. Wang, K. Trachenko, A. K. Soper, V. V. Brazhkin and S. Marinakis, *Phys. Rev. E*, **101**, 052109 (2020).
152. M. R. Stapleton, D. J. Tildesley, A. Z. Panagiotopoulos and N. Quirke, *Mol. Simul.*, **2**, 147 (1989).
153. B. Garzon, S. Lago, C. Vega, E. de Miguel and L. F. Rull, *J. Chem. Phys.*, **101**, 4166 (1994).
154. S. F. O'Shea, G. S. Dubey and J. C. Rasaiah, *J. Chem. Phys.*, **107**, 237 (1997).
155. A. L. Benavides, Y. Guevara and A. F. Estrada-Alexanders, *J. Chem. Thermodyn.*, **32**, 945 (2000).
156. A. L. Benavides, S. Lago, B. Garzon, L. F. Rull and F. D. Rio, *Mol. Phys.*, **103**, 3243 (2005).
157. B. M. Mognetti, L. Yelash, P. Virnau, W. Paul, K. Binder, M. Muller and L. G. MacDowell, *J. Chem. Phys.*, **128**, 104501 (2008).
158. B. Liu, J. W. Li, C. Qi, X. Q. Li, T. Y. Mai and J. Zhang, *RSC Adv.*, **7**, 50786 (2017).
159. J. M. Stubbs and J. I. Siepmann, *J. Chem. Phys.*, **121**, 1525 (2004).
160. G. Chatzis and J. Samios, *Chem. Phys. Lett.*, **374**, 187 (2003).
161. M. T. Oakley, H. Do and R. J. Wheatley, *Fluid Phase Equilib.*, **290**, 48 (2010).
162. H. Do, R. J. Wheatley and J. D. Hirst, *J. Phys. Chem. B*, **114**, 3879 (2010).
163. A. Liu and T. L. Beck, *J. Phys. Chem. B*, **102**, 7627 (1998).
164. J. Vrabec and J. Fischer, *Int. J. Thermophys.*, **17**, 889 (1996).
165. Y. F. Li, Y. X. Yu, Y. X. Zheng and J. D. Li, *Sci. China Chem.*, **55**,

1825 (2012).
166. M. Tafazzoli and A. Khanlarkhani, *J. Supercrit. Fluids*, **40**, 40 (2007).
167. I. Skarmoutsos and J. Samios, *J. Mol. Liq.*, **125**, 181 (2006).
168. C. G. Aimoli, E. J. Maginn and C. R. A. Abreu, *J. Chem. Eng. Data*, **59**, 3041 (2014).
169. M. Abbaspour and E. Nameni, *J. Supercrit. Fluids*, **74**, 61 (2013).
170. G. Guevara-Carrion, S. Ancherbak, A. Mialdun, J. Vrabec and V. Shevtsova, *Sci. Rep.*, **9**, 1 (2019).
171. S. D. Moon, *Bull. Korean Chem. Soc.*, **23**, 811 (2002).
172. T. Schnabel, A. Srivastava, J. Vrabec and H. Hasse, *J. Phys. Chem. B*, **111**, 9871 (2007),
173. Z. W. Li, S. H. Lai, W. Gao and L. P. Chen, *Russ. J. Phys. Chem. A*, **92**, 1332 (2018).
174. M. H. Zhang, M. B. Dou, M. Y. Wang and Y. Z. Yu, *J. Mol. Liq.*, **248**, 322 (2017).
175. M. P. E. Ishmael, L. B. Stutzman, M. Z. Lukawski, F. A. Escobedo and J. W. Tester, *J. Supercrit. Fluids*, **123**, 40 (2017).
176. H. Moradi, N. Rezamandi, H. Azizpour, H. Bahmanyar, K. Keynejad and Z. Nasrollahi, *Korean J. Chem. Eng.*, **39**, 717 (2022).
177. J. Shi, M. H. Zhang and X. Q. Dong, *Chem. J. Chin. Univ.*, **28**, 518 (2007).
178. J. Stoll, J. Vrabec and H. Hasse, *AIChE J.*, **49**, 2187 (2003).
179. B. Y. Wang and P. T. Cummings, *Int. J. Thermophys.*, **10**, 929 (1989).
180. M. Saharay and S. Balasubramanian, *J. Phys. Chem. B*, **110**, 3782 (2006).
181. I. Skarmoutsos, E. Guardia and J. Samios, *J. Chem. Phys.*, **133**, 014504 (2010).
182. S. Reiser, N. McCann, M. Horsch and H. Hasse, *J. Supercrit. Fluids*, **68**, 94 (2012).
183. W. H. Xu and J. C. Yang, *J. Phys. Chem. A*, **114**, 5414 (2010).
184. W. H. Xu, J. C. Yang and Y. Y. Hu, *J. Phys. Chem.*, **113**, 4781 (2009).
185. Z. H. Yang, M. Y. Li, B. Peng, M. Q. Lin and Z. X. Dong, *J. Dispersion Sci. Technol.*, **35**, 168 (2014).
186. I. Skarmoutsos, D. Dellis and J. Samios, *J. Chem. Phys.*, **126**, 224503 (2007).
187. Z. H. Yang, M. Y. Li, B. Peng, M. Q. Lin and Z. X. Dong, *J. Dispersion Sci. Technol.*, **35**, 143 (2014).
188. R. S. Chatwell, G. Guevara-Carrion, Y. Gaponenko, V. Shevtsova and J. Vrabec, *Phys. Chem. Chem. Phys.*, **23**, 3106 (2021).
189. E. Mareev, T. Semenov, A. Lazarev, N. Minav, A. Sviridov, F. Potemikin and V. Gordienko, *Molecules*, **25**, 5424 (2020).
190. H. Nishiumi, M. Fujita and A. Kenichi, *Fluid Phase Equilib.*, **117**, 356 (1996).
191. Y. He, M. H. Zhang, X. Q. Dong, *J. Chem. Eng. Chin. Univ.*, **22**, 152 (2008).
192. M. Tafazzoli and A. Khanlarkhani, *Chem. Phys. Lett.*, **458**, 308 (2008).
193. L. A. Ferreira Coelho, A. Marchut, J. V. de Oliveira and P. B. Balbuena, *Ind. Eng. Chem. Res.*, **39**, 227 (2000).
194. J. Zhou, X. H. Lu, Y. R. Wang and J. Shi, *Chem. J. Chin. Univ.*, **21**, 762 (2000).
195. J. Zhou, X. H. Lu, Y. R. Wang and J. Shi, *Fluid Phase Equilib.*, **172**, 279 (2000).
196. J. Y. Wang, H. M. Zhong, H. J. Feng, W. D. Qiu and L. P. Chen, *J. Chem. Phys.*, **140**, 104501 (2014).
197. N. Galand and G. Wipff, *New J. Chem.*, **27**, 1319 (2003).
198. Y. Iwai, Y. Mori and Y. Arai, *Fluid Phase Equilib.*, **167**, 33 (2000).
199. M. G. Martin and J. I. Siepmann, *J. Phys. Chem. B*, **102**, 2569 (1998).
200. T. Lafitte, A. Apostolakou, C. Avendano, A. Galindo, C. S. Adjiman, E. A. Muller and G. Jackson, *J. Chem. Phys.*, **139**, 154504 (2013).
201. I. Skarmoutsos and J. Samios, *J. Chem. Phys.*, **126**, 044503 (2007).
202. S. Shimizu and S. Abbott, *J. Phys. Chem. B*, **120**, 3713 (2016).
203. H. J. Feng, Z. F. Sun, B. X. Lei, G. N. Li and L. P. Chen, *J. Phys. Chem. B*, **117**, 12525 (2013).
204. J. Vrabec, Y. Huang and H. Hasse, *Fluid Phase Equilib.*, **279**, 120 (2009).
205. J. Chang, *Korean. J. Chem. Eng.*, **28**, 597 (2011).
206. J. Zhang, T. M. Fang and Y. F. Wang, *J. China Univ. Pet.*, **39**, 124 (2015).
207. D. Zabala, C. Nieto-Draghi, J. C. de Hemptinne and A. L. L. de Ramos, *J. Phys. Chem. B*, **112**, 16610 (2008).
208. J. Vorholz, V. I. Harismiadis and B. Rumpf, A. Z. Panagiotopoulos and G. Maurer, *Fluid Phase Equilib.*, **170**, 203 (2000).
209. Y. Liu, A. Z. Panagiotopoulos and P. G. Debenedetti, *J. Phys. Chem. B*, **115**, 6629 (2011).
210. G. A. Orozco, I. G. Economou and A. Z. Panagiotopoulos, *J. Phys. Chem. B*, **118**, 11504 (2014).
211. V. A. Glezakou, R. Rousseau, L. X. Dang and B. P. McGrail, *Phys. Chem. Chem. Phys.*, **12**, 8759 (2010).
212. M. Saharay and S. Balasubramanian, *Ind. J. Phys.*, **83**, 13 (2009).
213. M. Tafazzoli and A. Khanlarkhani, *Fluid Phase Equilib.*, **267**, 181 (2008).
214. Y. Danten, T. Tassaing and M. Besnard, *J. Mol. Liq.*, **117**, 49 (2005).
215. Y. Danten, T. Tassaing and M. Besnard, *J. Chem. Phys.*, **123**, 074505 (2005).
216. T. Kuznetsova and B. Kvamme, *Energy Conv. Manage.*, **43**, 2601 (2002).
217. O. A. Moultos, I. N. Tsimpanogiannis, A. Z. Panagiotopoulos, and I. G. Economou, *J. Phys. Chem. B*, **118**, 5532 (2014).
218. O. A. Moultos, G. A. Orozco, I. N. Tsimpanogiannis, A. Z. Panagiotopoulos and I. G. Economou, *Mol. Phys.*, **113**, 2805 (2015).
219. O. A. Moultos, I. N. Tsimpanogiannis, A. Z. Panagiotopoulos and I. G. Economou, *J. Chem. Thermodyn.*, **93**, 424 (2016).
220. B. L. Bhargava, M. Saharay and S. Balasubramanian, *Bull. Mat. Sci.*, **31**, 327 (2008).
221. X. H. Huang, C. J. Margulis, Y. H. Li and B. J. Berne, *J. Am. Chem. Soc.*, **127**, 17842 (2005).
222. B. L. Bhargava, A. C. Krishna and S. Balasubramanian, *AIChE J.*, **54**, 2971 (2008).
223. D. S. Firaha and B. Kirchner, *J. Chem. Eng. Data*, **59**, 3098 (2014).
224. H. Y. Zhu, Y. Li, H. G. Ren, D. Zhou and J. Z. Yin, *Chin. J. Chem. Eng.*, **27**, 2653 (2019).
225. H. Y. Zhu, Y. Li, D. Zhou, Q. Q. Xu and J. Z. Yin, *Colloid Surf. A-Physicochem. Eng. Asp.*, **603**, 125272 (2020).
226. W. B. Wang, J. Z. Yin, L. H. Sun and E. M. Feng, *Acta Phys. -Chim. Sin.*, **25**, 2291 (2009).
227. H. R. Ren, X. D. Liang, D. Zhou and J. Z. Yin, *Ind. Eng. Chem. Res.*, **56**, 3733 (2017).
228. B. Creton and V. Lachet, *Thermodynamic study of binary systems containing carbon dioxide and associated gases using molecular simulation techniques*, 14th Greenhouse Gas Control Technologies Conference Melbourne, 21 (2018).

229. A. J. Cresswell, R. J. Wheatley, R. D. Wilkinson and R. S. Graham, *Faraday Discuss.*, **192**, 415 (2016).
230. E. Bourasseau, V. Lachet, N. Desbiens, J.-B. Maillet, J.-M. Teuler and P. Ungerer, *J. Phys. Chem. B*, **112**, 15783 (2008).
231. V. Lachet, B. Creton, T. de Bruin, E. Bourasseau, N. Desbiens, O. Wilhelmsen and M. Hammer, *Fluid Phase Equilib.*, **322**, 66 (2012).
232. X. X. Jiang, G. Y. Chen, Y. T. Li, X. L. Cheng and C. M. Tang, *Chin. Phys. B*, **25**, 026102 (2015).
233. J. Xue, X. H. Nie, Z. Y. Du, H. R. Li, L. Zhao, Y. Zhu and J. J. Wang, *J. CO_2 Util.*, **55**, 101790 (2022).
234. Z. Y. Du, S. Deng, L. Zhao, X. H. Nie, S. J. Li, Y. Zhang, J. Zhao and N. Zheng, *J. CO_2 Util.*, **38**, 177 (2020).
235. J. M. Miguez, J. M. Garrido, F. J. Blas, H. Segura, A. Mejia and M. Pineiro, *J. Phys. Chem. C*, **118**, 24504 (2014).
236. V. K. Michalis, I. N. Tsimpanogiannis, A. K. Stubos and I. G. Economou, *Phys. Chem. Chem. Phys.*, **18**, 23538 (2016).
237. P. Kastanidis, V. K. Michalis, G. E. Romanos, A. K. Stubos, I. G. Economou and I. N. Tsimpanogiannis, *J. Chem. Eng. Data*, **63**, 1027 (2018).
238. L. L. Zhao, L. Tao and S. C. Lin, *Ind. Eng. Chem. Res.*, **54**, 2489 (2015).
239. B. Liu, J. Q. Shi, M. H. Wang, J. Zhang, B. J. Sun, Y. Shen and X. L. Sun, *J. Supercrit. Fluids*, **111**, 171 (2016).
240. S. Mohammed and G. A. Mansoori, *Energy Fuels*, **32**, 2095 (2018).
241. S. Mohammed and G. A. Mansoori, *Energy Fuels*, **32**, 5409 (2018).
242. Y. F. Yang, A. K. N. Nair, M. F. A. C. Ruslan and S. Y. Sun, *J. Phys. Chem. B*, **124**, 9556 (2020).
243. J. Xue, X. H. Nie, L. Zhao, R. Zhao, J. J. Wang, C. D. Yang and A. F. Lin, *J. Supercrit. Fluids*, **182**, 105533 (2022).
244. G. V. Mudzhikova and E. N. Broskava, *Colloid J.*, **77**, 306 (2015).
245. S. Salaniwal, S. T. Cui, H. D. Cochran and P. T. Cummings, *Langmuir*, **17**, 1773 (2001).
246. M. L. Alcantara, P. H. R. Silva, L. L. Romanielo, L. Cardozo-Filho and S. Mattedi, *J. Mol. Liq.*, **306**, 112775 (2020).
247. N. Sohrevardi, M. R. Bozorgmehr, M. M. Heravi and M. Khanpour, *J. Supercrit. Fluids*, **130**, 321 (2017).
248. X. M. Yang, J. X. Xu, S. H. Wu, M. Yu, B. Hu, B. Y. Cao and J. H. Li, *Int. J. Hydrog. Energy*, **43**, 10980 (2018).
249. X. M. Yang, Y. Y. Feng, J. X. Xu, J. H. Jin, Y. B. Liu and B. Y. Cao, *Appl. Therm. Eng.*, **162**, 114228 (2019).
250. X. M. Yang, C. C. Duan, J. X. Xu, Y. B. Liu and B. Y. Cao, *Int. J. Heat Mass Transf.*, **135**, 413 (2019).
251. Y. B. Liu and B. Y. Cao, *Int. J. Hydrog. Energy*, **45**, 4297 (2020).
252. D. T. Banuti, *J. Supercrit. Fluids*, **98**, 12 (2015).
253. H. S. Zhang, J. L. Xu and X. J. Zhu, *Acta. Phys. Sin.*, **70**, 044401 (2021).

Supporting Information

Comprehensive review on physical properties of supercritical carbon dioxide calculated by molecular simulation

Gaoliang Liao*,, Yuntao Du*,**, Feng Zhang*,**,†, and Jiaqiang E*,****

*College of Mechanical and Vehicle Engineering, Hunan University, Changsha 410082, China
**Institute of New Energy and Energy-saving & Emission-reduction Technology, Hunan University, Changsha 410082, China
(*Received 31 May 2022 • Revised 2 September 2022 • Accepted 11 October 2022*)

Table S1. Force field model comparison of AAD in predicting thermodynamic properties over 300-480 K, 500-680 K, 700-900 K temperature ranges at 20 K intervals

	T (K)	AAD (%)						
		ρ	α	κ_T	C_p	C_v	μ_{JT}	C_{sound}
Zhang	300-480	1.68	2.89	3.94	1.51	4.96	24.84	0.82
	500-680	1.98	1.17	1.09	1.07	1.58	6.41	0.87
	700-900	1.72	0.88	0.61	0.24	0.49	13.50	1.10
SAFT-γ	300-480	0.88	3.53	8.11	2.95	9.31	24.31	7.91
	500-680	0.56	2.46	1.14	0.42	2.54	20.05	2.13
	700-900	1.22	1.50	0.76	0.52	0.92	84.10	1.73
TraPPE	300-480	2.32	4.49	1.83	4.44	1.5	26.41	3.59
	500-680	2.95	0.97	0.74	0.50	0.63	6.04	2.26
	700-900	2.66	1.00	0.98	0.33	0.15	16.82	2.08
EPM2	300-480	2.45	5.82	5.18	2.81	3.39	30.04	1.35
	500-680	2.66	1.37	1.00	0.82	1.26	5.71	1.42
	700-900	2.23	1.19	0.82	0.20	0.37	22.74	1.54
PR	300-480	3.05	21.2	36.42	2.29	12.19	128.18	15.72
	500-680	1.54	2.42	7.00	0.95	3.61	26.00	4.58
	700-900	0.96	1.56	3.91	0.64	2.61	30.18	2.87

Data from the reference of Aimoli et al. [1] (see Table 4 in their paper)

Table S2. Comparison of saturation properties calculated by several models with NIST

	T (K)	ρ_l^a (kg/m^3)	ρ_v^a (kg/m^3)	P^b (MPa)
[c]Zhang	230	1,125.83	24.65	0.897
	240	1,087.67	34.74	1.288
	250	1,044.54	47.98	1.788
	260	998.13	65.29	2.413
	270	945.89	88.36	3.179
	280	883.84	121.52	4.108
	290	804.70	174.22	5.233
[c]EPM2	230	1,120.70	22.92	0.848
	240	1,081.29	32.55	1.224
	250	1,039.01	45.55	1.706
	260	992.85	63.35	2.318
	270	940.98	87.91	3.085
	280	878.54	122.90	4.032
	290	797.30	176.30	5.187

Table S2. Continued

	T (K)	ρ_l^a (kg/m^3)	ρ_v^a (kg/m^3)	P^b (MPa)
[c]MSM	230	1,119.62	23.23	0.835
	240	1,081.34	32.67	1.206
	250	1,040.54	45.13	1.680
	260	995.75	61.86	2.276
	270	944.72	85.02	3.014
	280	884.82	118.70	3.924
	290	808.85	170.30	5.042
[c]Errington	230	1,130.70	25.08	0.909
	240	1,091.02	35.38	1.311
	250	1,047.56	48.59	1.822
	260	1,000.97	65.88	2.456
	270	949.38	90.26	3.235
	280	886.09	128.40	4.197
	290	803.66	189.70	5.393
[c]TraPPE	230	1,127.11	19.10	0.710
	240	1,090.27	27.30	1.044
	250	1,050.96	38.09	1.476
	260	1,007.66	52.29	2.023
	270	958.73	71.33	2.701
	280	902.27	98.18	3.531
	290	832.83	140.00	4.549
[d]Yang et al.	228	1,109.60	19.68	0.760
	238	1,077.47	26.42	0.980
	248	1,044.03	38.53	1.490
	258	996.06	49.54	1.980
	268	956.46	65.81	2.620
	278	908.93	87.81	3.440
	288	847.77	115.09	4.500
[e]Nieto-Draghi et al.	216.6	1,168.60	16.57	0.630
	230		29.30	
	240	1,080.60	38.75	1.500
	260		80.90	
	270	937.10	102.00	3.700
	280		149.0	
	285	838.70	153.10	5.200
[f]Merker et al.	220	1,161.248	14.872	0.574
	230	1,121.208	22.22	0.866
	240	1,084.60	31.90	1.251
	250	1,042.36	44.704	1.752
	260	995.72	61.776	2.390
	270	944.24	84.832	3.190
	280	885.28	117.04	4.190
	290	809.60	161.92	5.350
	295	765.60	191.84	6.030
	300	708.40	232.32	6.730

[a] ρ_l and ρ_v are saturated liquid and vapor densities, respectively.

[b] P is the saturation pressure.

[c] Data from the reference of Zhang et al. [2] (see Table II to Table VI in their paper)

[d] Data from the reference of Yang et al. [3] (see Table 7 in their paper)

[e] Data from the reference of Nieto-Draghi et al. [4] (see Table II in their paper)

[f] Data from the reference of Merker et al. [5] (see Table I in supporting information of their paper)

Table S3. AAD comparison of temperature of each model at certain density or pressure

	ρ (kg/m^3) or P (MPa)	AAD (%)						
		TraPPE	EPM2	Zhang	Cygan	TraPPE-flex	Higashi	SAFT-γ
μ	200	15.51	14.82	13.81	8.53	9.12	9.16	15.87
	300	5.96	8.07	5.79	0.54	6.45	1.83	5.04
	400	5.53	1.62	5.05	3.78	4.69	3.31	9.06
	500	1.65	3.41	2.22	3.27	3.11	10.79	14.50
	600	2.76	2.32	2.68	2.95	6.87	7.98	17.81
	700	1.77	2.1	2.19	5.56	8.17	10.56	24.75
	800	3.47	3.35	0.75	7.21	7.85	13.11	34.42
	900	7.57	1.71	4.31	7.01	9.74	13.67	47.72
	1,000	11.75	5.04	2.05	6.81	12.93	12.80	55.99
	1,100	10.89	3.76	3.96	6.27	11.93	14.23	68.44
	1,200	7.51	2.88	4.55	5.16	11.75	13.55	93.02
	1,300	9.06	6.32	11.34	8.30	12.16	17.24	160.05
λ	200	59.32	58.47	59.61	39.74	39.05	76.01	72.11
	300	51.00	52.12	51.28	31.62	29.45	69.36	67.61
	400	39.91	39.09	40.16	14.31	12.93	59.72	55.77
	500	28.02	27.88	31.12	6.53	2.99	51.64	44.06
	600	22.88	25.81	28.96	9.57	13.81	48.51	39.99
	700	10.23	12.14	15.25	10.08	12.10	39.32	28.15
	800	6.13	7.30	8.63	15.38	19.22	33.33	19.32
	900	2.06	2.06	4.50	18.36	20.04	27.85	12.66
	1,000	6.97	2.89	2.67	25.31	24.33	23.12	5.23
	1,100	8.45	5.27	4.92	18.84	26.79	18.88	1.77
	1,200	11.50	8.83	9.32	22.35	27.01	15.44	11.46
	1,300	14.14	13.05	6.00	22.53	25.63	15.77	11.60
D	10 (MPa)	12.95	5.89	2.84	4.63	10.71	8.92	28.33
	20	11.34	6.40	2.20	5.00	8.22	9.02	26.26
	30	9.83	6.40	4.18	3.81	7.44	8.93	23.30
	50	16.05	9.71	6.83	8.95	12.63	14.35	31.75
	75	14.72	9.07	7.18	8.38	11.80	14.80	29.68
	88	16.68	12.44	10.58	11.69	14.17	16.67	31.23
	100	12.94	6.03	5.67	4.49	9.88	12.23	35.65
	125	7.72	3.27	3.34	2.09	4.03	8.68	27.86
	150	10.88	2.14	5.24	1.66	6.77	11.03	39.39
	200	11.88	3.35	5.00	2.84	7.78	13.39	45.82

Data from the reference of Aimoli et al. [6] (see Table 1 and Table 3 in supporting data of their paper)

Table S4. AAD comparison of temperature of each model at certain temperature

	T (K)	AAD (%)						
		TraPPE	EPM2	Zhang	Cygan	TraPPE-flex	Higashi	SAFT-γ
μ	273.15	13.07	1.10	3.67	4.69	15.44	18.29	99.80
	303.15	8.92	4.28	6.15	5.80	11.92	12.29	53.93
	328.15	8.01	4.85	4.96	6.39	8.72	12.88	45.64
	473.15	5.50	4.91	3.86	6.10	7.85	9.43	44.31
	573.15	5.18	5.85	5.62	4.53	6.68	7.74	43.56
λ	273.15	11.02	6.39	1.04	24.82	24.74	20.31	8.55
	303.15	23.37	20.24	21.16	26.70	28.53	39.37	30.19
	328.15	21.28	20.80	21.88	21.61	21.19	40.52	30.01
	473.15	19.92	21.76	22.26	16.33	19.36	37.30	29.14
	573.15	20.28	20.33	21.31	15.42	19.20	39.07	30.27
D	273	15.11	4.47	6.71	3.73	10.20	14.05	45.54
	298	11.97	4.14	2.37	3.73	9.57	12.24	38.60
	333	11.34	3.56	4.22	2.36	7.41	9.98	33.09
	373	11.40	4.65	4.14	3.55	8.24	10.85	31.17
	424	10.57	6.70	5.83	5.19	7.42	10.18	28.59
	450	15.29	10.57	8.45	9.51	12.28	15.31	32.25

Data from the reference of Aimoli et al. [6] (see Table 1 and Table 3 in supporting data of their paper)

Table S5. Global AAD comparison of transport properties predicted by 7 models

	AAD (%)						
	TraPPE	EPM2	Zhang	Cygan	TraPPE-flex	Higashi	SAFT-γ
μ	7.32	4.69	4.99	5.62	9.2	11.13	50.81
λ	20.31	19.65	20.02	20.13	22.03	37.55	28.18
D	12.56	5.87	5.35	4.85	9.19	12.08	34.34

Data from the reference of Aimoli et al. [6] (see Table 1 and Table 3 in supporting data of their paper)

REFERENCES

1. C. G. Aimoli, E. J. Maginn and C. R. A. Abreu, *Fluid Phase Equilib.*, **368**, 80 (2014).
2. Z. G. Zhang and Z. H. Duan, *J. Chem. Phys.*, **122**, 214507 (2005).
3. Z. Yang, M. Q. Gong, Y. Zhou, X. Q. Dong, X. D. Li, H. Y. Li and J. F. Wu, *Sci. China Tech. Sci.*, **58**, 650 (2015).
4. C. Nieto-Draghi, T. de Bruin, J. Perez-Pellitero, J. B. Avalos and A. D. Mackie, *J. Chem. Phys.*, **126**, 064509 (2007).
5. T. Merker, C. Engin, J. Vrabec and H. Hasse, *J. Chem. Phys.*, **132**, 234512 (2010).
6. C. G. Aimoli, E. J. Maginn and C. R. A. Abreu, *J. Chem. Phys.*, **141**, 134101 (2014).